2009-07-10

Offset QPSK in SISO and MIMO Environments

Xiaoyu Dang
Brigham Young University - Provo

OFFSET QPSK IN SISO AND MIMO ENVIRONMENTS

by

Xiaoyu Dang

A dissertation submitted to the faculty of

Brigham Young University

in partial fulfillment of the requirements for the degree of

Doctor of Philosophy

Department of Electrical and Computer Engineering

Brigham Young University

August 2009

BRIGHAM YOUNG UNIVERSITY

GRADUATE COMMITTEE APPROVAL

of a dissertation submitted by

Xiaoyu Dang

This dissertation has been read by each member of the following graduate committee and by majority vote has been found to be satisfactory.

Date	Michael D. Rice, Chair
Date	Richard W. Christiansen
Date	Brian D. Jeffs
Date	Wynn C. Stirling
Date	Karl F. Warnick

BRIGHAM YOUNG UNIVERSITY

As chair of the candidate's graduate committee, I have read the dissertation of Xiaoyu Dang in its final form and have found that (1) its format, citations, and bibliographical style are consistent and acceptable and fulfill university and department style requirements; (2) its illustrative materials including figures, tables, and charts are in place; and (3) the final manuscript is satisfactory to the graduate committee and is ready for submission to the university library.

Date

Michael D. Rice
Chair, Graduate Committee

Accepted for the Department

Michael J. Wirthlin
Graduate Coordinator

Accepted for the College

Alan R. Parkinson
Dean, Ira A. Fulton College of
Engineering and Technology

ABSTRACT

OFFSET QPSK IN SISO AND MIMO ENVIRONMENTS

Xiaoyu Dang

Department of Electrical and Computer Engineering

Doctor of Philosophy

We demonstrate how the performance of offset quadrature phase-shift keying (OQPSK) and its variants of Feher-patented QPSK (FQPSK) and Shaped Offset QPSK (SOQPSK) (collectively known as the ARTM Tier-1 waveforms) in single input single output (SISO) system could change with the channel fading parameters. The bit error rate expression of offset QSPK and ATRM Tier-1 waveforms over the aeronautical telemetry multipath channel has been derived. Simulations show that for the case of a single multipath ray, the BER gets worse with increasing Γ for a fixed delay, and that the BER has a quasi-periodic property for fixed Γ and increasing τ. For the case of two multipath rays, the multipath component characterized by large amplitude and small delay is the main factor of the BER degradation, while the BER is not very sensitive to the change of multipath delay. Analysis of the average bit error probability shows that a relatively high error floor at approximately 10^{-2} occurs for $|\Gamma_1| \geq 0.5$.

When offset quadrature phase-shift keying (OQPSK) is used in multiple input multiple output (MIMO) environment, orthogonal space-time block codes can be

applied *to waveforms* to orthogonalize a space-time coded multiple-input, multiple-output link. For offset QPSK, this technique has the advantage of eliminating the I/Q interference associated with simultaneous transmission of offset QPSK waveforms. In addition, orthogonalization presents uncorrelated noise samples to the space-time trellis decoder. As a consequence, a less complex space-time decoder (relative to what would be required without orthogonalization) can be used.

It is demonstrated that a concatenated system based on an orthogonal space-time block code and a trellis code, optimized for single-input, single-output fading channel, outperforms a space-time trellis code for a 2×1 system. The space-time block code orthogonalizes the channel seen by the outer code and this simplifies the computations required for decoding. The advantages of orthogonalization are achieved at the expense of rate. In the examples presented, the codes were chosen to have roughly equivalent bit error rate performance and identical code rates: the complexity was compared.

ACKNOWLEDGMENTS

I would like to express my gratitude to all those who gave me the possibility to complete this dissertation.

My heartfelt thanks goes to Dr. Michael Rice, my Ph.D. Advisor, Mentor, and Committee Chairman, who guided me with intelligence and expertise which, with each meeting, shed more and more light on my dissertation path.

I furthermore want to thank the other four members of my committee: Dr. Richard Christiansen, Dr. Brian Jeffs, Dr. Wynn Stirling, and Dr. Karl Warnick for their wholesome advice. Also, I would thank Dr. Michael Jensen for the recent discussions.

Finally, I want to thank Dr. Michael Rice and Edward Air Force Base and Department of Defense for their generous research funding support. I would like thank the Electrical and Computer Engineering department, Brigham Young University, for their consistent financial support.

Table of Contents

List of Tables

List of Figures

Chapter 1

Introduction

1.1 Background and Motivation

Modulation techniques like binary phase-shift keying (BPSK), quadrature phase-shift keying (QPSK), and offset QPSK (also known as staggered) are well-known continuous phase modulation techniques for wireless transmission in which information bits or symbols are mapped onto modulation constellation points to be transmitted over the channel. BPSK maps binary information bits from $\{0, 1\}$ to $\{-1, 1\}$, and QPSK maps quaternary symbols from $\{i = 0, 1, 2, 3\}$ to $\{\exp(j(i\pi/2 + \pi/4)), i = 0, 1, 2, 3\}$. OQPSK (offset QPSK) is a special version of QPSK in which the transmitted signal has two orthogonal BPSK modulations with a half symbol duration offset. This offset technique is to overcome the disadvantage of a amplitude modulation resulting from 180^o phase shift with a nonlinear RF power amplifier. The incoming signal is divided in the modulator into two parts, I and Q, which are then transmitted shifted by a half symbol duration so that the phase change is no more than 90 degrees. The constant envelope is needed [4] to avoid spectral spreading due to the nonlinearity at the power amplifier at the transmitter.

There are two variants of OQPSK specified in IRIG 106 [5]: Feher-patented QPSK (FQPSK) [6] and a compatible variant of the MIL-STD 188-181 Shaped Offset QPSK (SOQPSK) [7]. These two modulation formats, known collectively as ARTM Tier-1 Waveforms, have twice the spectral efficiency as PCM/FM [8], even when used with non-linear power amplifiers. The FQPSK and SOQPSK are fully compatible with the OQPSK detector, i.e., the integrate & dump detector.

While there are simulations and experiments of ARTM Tier-1 modulations investigated in literature [6] [7] over additive white Gaussian noise (AWGN) channel,

the performance over aeronautical telemetry channel is of interest. The aeronautical telemetry channel is described as a frequency selective fading channel in [9], the multipath interference has become increasingly frequency selective and has proved to be the dominant channel impairment.

As a modulation format for single input and single output (SISO), the application of OQPSK and its variants to multiple input multiple output (MIMO) introduces new challenges. The space-time coding techniques in MIMO [10] [11], [2] are now attracting more and more attention, for it has the advantage of increased channel capacity and diversity gain. When OQPSK is applied to multiple input multiple output (MIMO) environment, the known space time orthogonal block code cannot be applied directly on the symbol level [1] [12].

In each of the subsection below, the SISO aeronautical telemetry channel and the space-time MIMO environment are introduced.

1.1.1 Multipath Model in SISO Aeronautical Telemetry Channel

Similar to most wireless communication links, multipath channel interference is found to be the dominant cause of signal outages in aeronautical telemetry [13] [9]. Typical multipath interference occurs when multiple copies of the transmitted signal arrive at the receiver. The multiple copies are generated by reflections from the physical environment, most notably the terrain, and are a function of the geometry defined by the locations of the transmitter, receiver, and reflectors. Previous work on channel modeling at L- and S-bands at Edwards AFB [13] showed that a good model for the multipath interference is a linear system with impulse response

$$h(t) = \delta(t) + \sum_{i=1}^{N_r} \Gamma_i \delta(t - \tau_i). \tag{1.1}$$

The first term on the right-hand-side corresponds to line-of-sight propagation which has been normalized to zero delay and unit amplitude. The second and third terms on the right-hand-side correspond to reflections with amplitudes Γ_1 and Γ_2, and delays τ_1

and τ_2. The properties of these model parameters for L- and S-band and reasonably well understood and are described in [9].

Most published literature on FQPSK and SOQPSK are over Gaussian channel. The initial FQPSK was in [14] and the enhanced FQPSK [4] viewed as cross-correlated trellis-coded quadrature modulation (XTCQM) was developed to improve the spectral shape. Error performance analysis of FOQSK was also provided in [4]. SOQPSK was put forward in [7], and performance analysis of the integrated and dump (I&D) detector, fully compatible with OQPSK receiver, were reported in [15, 16]. A near optimum common detector based on XTCQM for FQPSK and SOQPSK are in [17].

The focus of our work is to explore the influence on BER with the change of multipath parameters. Our emphasis is the setup of the BER analysis model, calculation and simulation for OQPSK, FQPSK and SOQPSK as shown in Chapter 2 and Chapter 3.

1.1.2 Space-time Coded Offset QPSK in MIMO

Alamouti invented the simplest STBC [10] in 1998, It takes two time-slots from 2 transmit antennas to transmit two symbols.

$$\mathbf{S} = \begin{bmatrix} s_1 & s_2^* \\ s_2 & -s_1^* \end{bmatrix} \tag{1.2}$$

where the two transmit antenna transmit s_1 and s_2 separately during the first time-slot, then transmit s_2^*, $-s_1^*$ separately during the follwing time-slot.

The received signal of two time-slots will be stacked as

$$\mathbf{Y} = \mathbf{HS} + \mathbf{N} = \begin{bmatrix} y_1 \\ y_2^* \end{bmatrix} = \begin{bmatrix} h_1 & h_2 \\ h_2^* & -h_1^* \end{bmatrix} \begin{bmatrix} s_1 \\ s_2 \end{bmatrix} + \begin{bmatrix} n_1 \\ n_2^* \end{bmatrix}. \tag{1.3}$$

Alamouti scheme orthogonalizes the wireless link by multiplying both sides of equation (1.3) by $\mathbf{H}^H$ to make the channel gain real.

$$\mathbf{Z} = \mathbf{H}^H\mathbf{Y} = \mathbf{H}^H\mathbf{H}\mathbf{S} + \mathbf{H}^H\mathbf{N} = \begin{bmatrix} |h_1|^2 + |h_2|^2 & 0 \\ 0 & |h_1|^2 + |h_2|^2 \end{bmatrix} \begin{bmatrix} s_1 \\ s_2 \end{bmatrix} + \begin{bmatrix} v_1 \\ v_2^* \end{bmatrix} \quad (1.4)$$

where the noise is still white Gaussian

$$\begin{bmatrix} v_1 \\ v_2^* \end{bmatrix} = \begin{bmatrix} h_1^* & h_2* \\ h_2 & -h_1 \end{bmatrix} \begin{bmatrix} n_1 \\ n_2^* \end{bmatrix}. \quad (1.5)$$

When Alamouti scheme was put forward, BPSK or QPSK was assumed. Offset modulations such as OQPSK and GMSK have better spectral benefits than non-offset modulations, when used with a non-linear power amplifier. Because of the offset in inphase and quadrature modulation, the receive signal is sampled at 1 sample per bit interval, the I/Q interference is unavoidable and the noise is no longer white [1]. In [3], The Alamouti space-time block code was put forward in *waveform* format so that the channel gain is still real and optimum SISO detector can be used for each received antenna. Direct use of the Alamouti space-time block code with OQPSK is investigated by [12].

Tarokh's seminal paper [2] introduced a new category codes called space-time trellis codes (STTC) for high data rate wireless communication, where the rank criteria and the determinant criteria were made for the selection of good codes. The default modulation scheme here were still BPSK, QPSK and 8PSK. Offset modulations have seldom been discussed with STTC. In [1], a STTC with delay diversity was discussed with MSK, a variant of OQSPK. When OQPSK is treated as a special continuous phase modulation (CPM), a space-time code cannot be applied directly to the symbols because there is no way to preserve the continuous phase property and the associated memory in the data symbol sequence [18, 19]. Application of space-time trellis codes for general CPM has been investigated by Zhang and Fitz [18], Aygolu and Celebi [20].

With the development of STBC and STTC, there were a number of published results on the concatenation of these techniques in literature.

Let us first look at the concatenation of STBC as the inner encoder and STTC or TCM as the outer encoder. Jafarkhani et al [21] described a system using a space-time trellis outer code with an inner space-time orthogonal block code which provided better coding gain and kept the same diversity gain as in contrast to the simple STTC. Similarly, Wiwamogsatham [22] used STBC as the inner code and multi-dimensional TCM as the outer code for the concatenation. The design of the optimum M-TCM with the inner STBC encoder was investigated. While both papers used the STBC as the inner encoder, the orthogonality of the STBC could not be extended to simplify the complex channel as initially shown in [10]. The received signals were still the complex multiplication of the transmitted signal and the channel plus noise.

To further exploit the advantage of STBC orthogonality, there were increased interests on schemes using STBC as an outer coder and various inner coders like BICM, turbo code, and trellis coded modulation (TCM). While keeping the space-time as an outer coder, bit interleaved coded modulation (BICM) was considered as an outer encoder in [23]. BICM is a technique that makes bits in any code word fade independently, which is implemented by a bit-wise interleaver before the bits are mapped onto the constellation points in the signal set. An upper bound on bit error rate for a MIMO system was derived in [23], which was based on expurgated bound of BICM. Besides BICM, Page [24] described a system using a space-time block code as the outer code and a turbo code as the inner code. This paper discussed how the optimum receiver was derived through least mean square criterion and how the optimum performance could be achieved through turbo decoders.

Still with the same outer code, a scheme using TCM as the inner code was described by Gong et al [25], where the design criterion and rules were detailed. Their scheme had better performance than some STTCs under the same spectral efficiency, signal constellation, and trellis complexity. In this scheme, a SISO TCM with the constellation of QPSK or 8-PSK was used. The TCM trellis encoder had only one symbol from QPSK or 8-PSK constellations for each encoder/branch output, which

led to a code rate change between TCM encoder and STBC encoder; i.e. a serial to parallel converter to change from the single symbol output of TCM encoder to two symbols input for the following STBC. The lower throughput was 1.5 bits per channel use. The case of 2 bits per channel use were also examined.

Teng [26] described a concatenated system with a TCM as the inner code and a space-time block code as the outer code in MIMO OFDM. They also showed that a concatenated system with inner SISO TCM and outer STBC will outperform some STTC. The inner SISO TCM coder was a coded QPSK, and the outer code was STBC. The throughput was 2 bits per channel use. The channel was assumed to be a three-path Rayleigh fading channel.

Aksoy and Aygolu [27] described a concatenated system which consisted of an inner trellis encoder and a coordinate interleaved space-time block code as the outer code for MIMO OFDM. By means of *coordinate interleaved*, a time-variant coefficient $e^{j\theta}$ was inserted before the conventional interleaver to bring some enhanced diversity. Performance criteria for this scheme were derived and simulations were provided to show the enhanced diversity.

All the concatenation schemes above are for non-offset modulations, due to the offset format in QPSK, the direct application of the discussed concatenated schemes above to OQPSK would be very difficult. The detector would have unavoidable inter-symbol interference at the receiver as shown in [1]. Our concatenated system is based on the outer STBC encoder and inner STTC encoder exclusively for offset QPSK are discussed in Chapter 4. The scheme where the Alamouti STBC is applied as an outer encoder for *packets (waveforms)* to overcome the limits due to the offset format. We describe a concatenation with the Alamouti STBC code as an outer encoder and a trellis code as an inner encoder for OQPSK. The advantage of eliminating the I/Q interference, keeping the noise white and simplifying a receiver detector is discussed in detail.

Compared with concatenated systems and STTC in [25] [26], our work is set up differently. First, our trellis structure of TCM is different. Both inner encoders previously mentioned were SISO TCM encoders, where each trellis branch output

was a single symbol and a rate change of the code was implied before entering STBC encoder, while our encoder is a two dimensional *space-time* TCM encoder, which has the trellis branch output of a vector of two symbols from the modulation constellation. Second, both modulation constellations mentioned were QPSK and 8-PSK, while we use 16 QAM in our space-time TCM scheme to match the spectral efficiency of a system based on a single STTC. This was done to make the performance comparison fair. Third, we tried to make the comparison not only with the regular STTC [25] [26], but with Tarokh's *smart-greedy* trellis. The STTC compared in [25] [26] was Tarokh's delay-diversity regular trellis which worked at 2 bits per channel use. That was to say, the STTC they used only have space expansion but no time expansion for each branch output. We include the comparison of our concatenated system with Tarokh's *smart-greedy* trellis, where each trellis output is a 2×2 matrix with both space and time expansion. This let our comparison scheme operate a 1 bit per channel use which they did not have. Fourth, based on our setup, we compare the implementation complexity by counting the real multipliers needed, which is to view these systems from a new angle.

Given the advantages of orthogonalization and the associated rate penalty, there is an open question as to whether the concatenated trellis-coded orthogonal space-time coded (CTO) system outperforms an STTC system at the same throughput. In Chapter 5, we demonstrate that for a given rate, two transmit antennas, and one receive antenna, the CTO system outperforms the STTC system both in terms of power and complexity. For the throughput at 1 bps per channel use, we made comparison between the BER bound of the concatenated inner STTC with outer STBC, and that of Tarokh's smart-greedy STTC [2]. And for the throughput at 2 bps per channel use, we compared the BER bound of *space-time* trellis coded 16 QAM with Tarokh's regular STTC.

1.2 Contributions

1. Bit error rate performance of Offset QSPK, FQPSK and SOQPSK.

The bit error rate of the analysis of QSPK, FQPSK and SOQPSK over the aeronautical telemetry multipath channel has been derived. Simulations show that for the case of a single multipath ray, the BER gets worse with increasing Γ for a fixed delay, and that the BER has a quasi-periodic property for fixed Γ and increasing τ. For the case of two multipath rays, the multipath component characterized by large amplitude and small delay is the main factor of the BER degradation, while the BER is not very sensitive to the change of multipath delay. A conference paper [29] has been published and a journal paper [30] has been published based on this work.

2. A concatenated system with space-time block code as an outer code and space-time trellis-coded offset-QPSK as an inner code in MIMO environment.

   We have shown how orthogonal space-time block codes can be applied *to waveforms* to orthogonalize a space-time coded multiple-input, multiple-output link. For offset QPSK, this technique has the advantage of eliminating the I/Q interference associated with simultaneous transmission of offset QPSK waveforms. In addition, orthogonalization presents uncorrelated noise samples to the space-time trellis decoder. As a consequence, a less complex space-time decoder (relative to what would be required without orthogonalization) can be used. These benefits are achieved at the expense of data rate as described. Also the optimum STTC-trellis code is based on waveform orthogonalization, which is the direct extension of the available optimum of SISO codes to MISO or MIMO environments. A conference paper [31] has been published based on this work.

3. Performance and complexity comparison between space-time trellis codes and concatenated trellis-coded orthogonal space-time block codes.

   This part answers an open question as to whether the concatenated trellis-coded orthogonal space-time coded (CTO) system outperforms an STTC system. We demonstrate that for a given rate, two transmit antennas, and one receive antenna, the CTO system outperforms the STTC system both in terms of power and complexity. A conference paper [32] has been submitted based on this work.

1.3 Organization

The remainder of this dissertation is organized as follows:

Chapter 2 gives error performance offset QPSK in multipath environment. Based on the aeronautical telemetry selective fading channel model, the analysis of the bit error rate performance is found to be closely related to the channel parameters.

Chapter 3 shows the error performance of Feher's QPSK (FQPSK) and Shaped Offset QSPK (SOQPSK). The trellis relationship of FQPSK signal sets are developed, and analysis, calculation, and simulation results show it has an error performance floor with the selective channel fading parameters.

Chapter 4 presents a concatenated system with space-time block code as an outer code and space-time trellis-coded offset-QPSK as an inner code. The introduction of the concatenated system is to overcome the inherent inter-symbol interference ISI problem of space-time trellis coded MSK [1]. We show the choice of the known optimum SISO trellis code can be the optimum inner space-time trellis code in the concatenated system.

Chapter 5 compares the performance and complexity of space-time trellis codes and concatenated trellis-coded orthogonal space-Time block codes. Given the advantages of orthogonalization and the associated rate penalty, there is an open question as to whether the concatenated system outperforms an STTC system. We demonstrate that for a given rate, two transmit antennas, and one receive antenna, the CTO system outperforms the STTC system both in terms of power and complexity.

Chapter 6 is the conclusion and future work.

Chapter 2

Error Performance of Offset QPSK in Multipath

For wireless communications with significant power and bandwidth constraints, Offset QPSK (OQPSK) are preferred for use with RF power amplifiers operating in full saturation. In this modulation format, the data is placed alternately on the I branch (for "in phase") and the Q branch ("phase quadrature"). A single phase transition can never exceed 90 degrees. This property contrasts OQPSK with conventional quadrature phase-shift keying (QPSK), in which the phase can sometimes change by 180 degrees (two 90-degree shifts in a single transition)

Since the FQPSK and SOQPSK are both compatible with the OQPSK receiver, the Integrate & Dump receiver, we start this chapter with the analysis of the transmitted OQPSK signal.

2.1 Bit Error Rate Analysis

Let $s(t)$ be the complex baseband representation of the transmitted offset QPSK (OQPSK) signal. The OQPSK signal can be represented by

$$s(t) = \sum_{n=0}^{\infty} \left(a_n p(t - nT_s) + j b_n p(t - \frac{1}{2}T_s - nT_s) \right) \tag{2.1}$$

where a_n, b_n are respectively the real and imaginary parts of OQPSK symbols s_n, $s_n \in \{\pm 1 \pm j\}$. $p(t)$ is the unit energy pulse shape with support on $-LT_s \leq t \leq LT_s$, and T_s is the symbol time in seconds.

The optimum detector is a matched-filter detector illustrated in Figure 2.1. The inphase and quadrature components of the received signal $I(t)$ and $Q(t)$ are filtered by a filter whose impulse response is a time-reversed copy of the pulse shape:

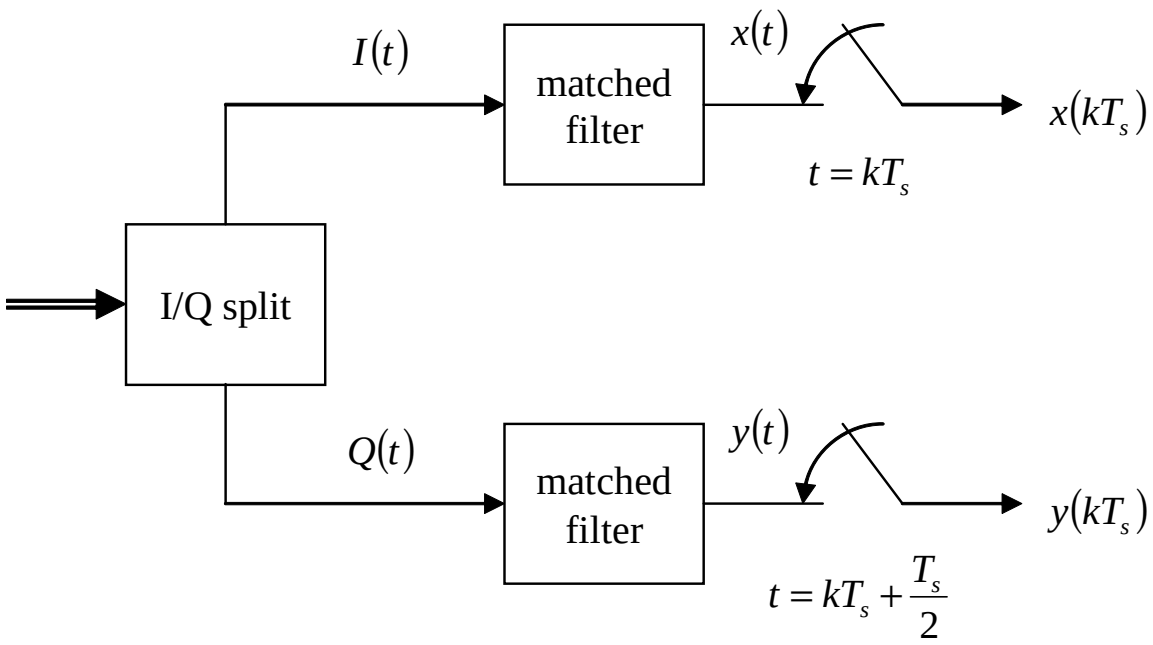

Figure 2.1: Optimum detector of OQPSK Signals

$h_{\mathrm{MF}} = p(-t)$. The output of the inphase matched filter, $x(t)$, is sampled at $t = kT_s, k = 0, 1, 2, \cdots$, to produce an estimate of a_k while the output of the quadrature matched filter, $y(t)$, is sampled at $t = kT_s + \frac{1}{2}T_s, k = 0, 1, 2, \cdots$, to produce an estimate of b_k.

The aeronautical telemetry channel may be modeled as a multipath channel with complex baseband impulse response [9]

$$h(t) = \delta(t) + \sum_{i=1}^{N_r} \Gamma_i \delta(t - \tau_i) \tag{2.2}$$

where $\Gamma_i, \tau_i, i = 1, \cdots N_r$ are the complex amplitude and delay of the i multipath propagation path, and N_r is the number of the multipath rays. Note that channel normalizes the gains and delays to the line-of-sight propagation path so that the line-of-sight propagation path has unit amplitude and zero delay. The received signal $r(t)$

may be represented as

$$r(t) = s(t) * h(t) + w(t) \tag{2.3}$$

$$= s(t) + \sum_{i=1}^{N_r} \Gamma_i s(t - \tau_i) + w(t) \tag{2.4}$$

where $w(t) = w_I(t) + jw_Q(t)$ represents the additive noise which is modeled as a complex Gaussian random process with zero mean and where the real and imaginary parts have power spectral density $\frac{N_0}{2}$ Watts/Hz.

Substituting (2.1) into (2.4) and solving collecting the real and imaginary components produces:

$$I(t) = \sum_{n=0}^{\infty} \left(a_n p(t - nT_s) + \sum_{i=1}^{N_r} \Re\{\Gamma_i\} a_n p(t - nT_s - \tau_i) \right.$$
$$\left. - \sum_{i=1}^{N_r} \Im\{\Gamma_i\} b_n p(t - nT_s - \frac{1}{2}T_s - \tau_i) \right) + w_I(t), \tag{2.5}$$

and

$$Q(t) = \sum_{n=0}^{\infty} \left(b_n p(t - nT_s - \frac{1}{2}T_s) + \sum_{i=1}^{N_r} \Re\{\Gamma_i\} b_n p(t - nT_s - \frac{1}{2}T_s - \tau_i) \right.$$
$$\left. + \sum_{i=1}^{N_r} \Im\{\Gamma_i\} a_n p(t - nT_s - \tau_i) \right) + w_Q(t) \tag{2.6}$$

where $\Re\{Z\}$ denotes the real part of Z and $\Im\{Z\}$ denotes the imaginary part of Z.

The matched filter output $x(t) = I(t) * p(-t)$ may be expressed as

$$x(t) = \sum_{n=0}^{\infty} \left(a_n R_p\left(t - nT_s\right) + \sum_{i=1}^{N_r} \Re\{\Gamma_i\} a_n R_p\left(t - nT_s - \tau_i\right) \right.$$
$$\left. - \sum_{i=1}^{N_r} \Im\{\Gamma_i\} b_n R_p\left(t - nT_s - \frac{1}{2}T_s - \tau_i\right) \right) + v_I(t), \tag{2.7}$$

and

$$y(t) = \sum_{n=0}^{\infty} \left(b_n R_p \left(t - nT_s - \frac{1}{2}T_s \right) + \sum_{i=1}^{N_r} \Re\{\Gamma_i\} b_n R_p \left(t - nT_s - \frac{1}{2}T_s - \tau_i \right) + \sum_{i=1}^{N_r} \Im\{\Gamma_i\} a_n R_p \left(t - nT_s - \tau_i \right) \right) + v_Q(t) \quad (2.8)$$

where $R_p(\cdot)$ is the deterministic pulse correlation function

$$R_p(\tau) = \int_{-\infty}^{\infty} p(t)p(t-\tau)dt. \quad (2.9)$$

The noise terms are

$$v_I(t) = \int_{-\infty}^{\infty} w_I(\lambda)p(\lambda - t)d\lambda, \quad (2.10)$$

and

$$v_Q(t) = \int_{-\infty}^{\infty} w_Q(\lambda)p(\lambda - t)d\lambda. \quad (2.11)$$

The output of the inphase matched filter $x(t)$ is sampled at $t = kT_s, k = 0, 1, 2, \cdots$, to produce

$$x(kT_s) = \sum_{n=0}^{\infty} \left[a_n R_p \left((k-n)T_s \right) + \sum_{i=1}^{N_r} \Re\{\Gamma_i\} a_n R_p \left((k-n)T_s - \tau_i \right) - \sum_{i=1}^{N_r} \Im\{\Gamma_i\} b_n R_p \left((k-n)T_s - \frac{1}{2}T_s - \tau_i \right) \right] + v_I(kT_s). \quad (2.12)$$

To simplify the equation above, let $T_s = 1$. It can be re-expressed as

$$x(k) = a_k R_p(0) + \sum_{n=0, n\neq k}^{\infty} a_n R_p(k-n) + \sum_{i=1}^{N_r} \sum_{n=0}^{\infty} \Re\{\Gamma_i\} a_n R_p(k-n-\tau_i) - \sum_{i=1}^{N_r} \sum_{n=0}^{\infty} \Im\{\Gamma_i\} b_n R_p \left(k-n-\frac{1}{2}-\tau_i \right) + v_I(k) \quad (2.13)$$

where $v_I(k)$ is a zero mean Gaussian random variable with variance $\frac{N_0}{2}$. If the pulse shape $p(t)$ satisfies the Nyquist no-ISI condition [4], then

$$R_p(k) = \begin{cases} 1 & k = 0 \\ 0 & k \neq 0 \end{cases} \tag{2.14}$$

and the first term in the first summation of (2.13) disappears. The terms in the first summation of (2.13) can be thought of as intersymbol-interference while the term in the second and third double summations can be thought of as cross-channel interference (or I-Q coupling caused by the phase shifts of the multipath propagation paths).

Following the same procedure for the quadrature matched filter output, $y(t)$ is sampled at $t = k + \frac{1}{2}, k = 0, 1, 2, \cdots$, to produce

$$\begin{aligned} y\left(k+\frac{1}{2}\right) = b_k R_p(0) + \sum_{n=0, n\neq k}^{\infty} b_n R_p(n-k) + \sum_{i=1}^{N_r}\sum_{n=0}^{\infty} \Re\{\Gamma_i\} b_n R_p(k-n-\tau_i) \\ + \sum_{i=1}^{N_r}\sum_{n=0}^{\infty} \Im\{\Gamma_i\} a_n R_p\left(k-n-\frac{1}{2}-\tau_i\right) + v_Q\left(k+\frac{1}{2}\right) \end{aligned} \tag{2.15}$$

where $v_Q(k+\frac{1}{2})$ is a zero mean Gaussian random variable with variance $\frac{1}{2}N_0$.

Before using standard techniques for error rate analysis, let us define the following variables generated by multipath effects. Let $\boldsymbol{\tau} = [\tau_1, \tau_2, \cdots, \tau_{N_r}]$ be the delay vector, $\boldsymbol{\Gamma} = [\Gamma_1, \Gamma_2, \cdots, \Gamma_{N_r}]$ be the complex coefficient vector, and

$$s(k, \tau_i) = \left[s_{k-\lfloor\tau_i\rfloor-2L}, s_{k-\lfloor\tau_i\rfloor-2L+1}, \cdots, s_{k-\lfloor\tau_i\rfloor+2L-1} \right], i = 1, \cdots, N_r. \tag{2.16}$$

Using these vector definitions, we make the following definitions:

$$\mathbf{s}(k,\boldsymbol{\tau}) = \left[s(k,\tau_1), s(k,\tau_2), \cdots, s(k,\tau_{N_r})\right], \tag{2.17}$$

$$M_{Ia}\Bigg(\mathbf{s}(k,\boldsymbol{\tau}),\boldsymbol{\Gamma},\boldsymbol{\tau},L\Bigg) = \sum_{i=1}^{N_r}\sum_{n=k-\lfloor\tau_i\rfloor-2L}^{k-\lfloor\tau_i\rfloor+2L-1} \Re\{\Gamma_i\}a_n R_p\left((k-n)-\tau_i\right), \tag{2.18}$$

$$M_{Ib}\Bigg(\mathbf{s}(k,\boldsymbol{\tau}),\boldsymbol{\Gamma},\boldsymbol{\tau},L\Bigg) = -\sum_{i=1}^{N_r}\sum_{n=k-\lfloor\tau_i+\frac{1}{2}\rfloor-2L}^{k-\lfloor\tau_i+\frac{1}{2}\rfloor+2L-1} \Im\{\Gamma_i\}b_n R_p\left(\left(k-n-\frac{1}{2}\right)-\tau_i\right), \tag{2.19}$$

$$M_{Qb}\Bigg(\mathbf{s}(k,\boldsymbol{\tau}),\boldsymbol{\Gamma},\boldsymbol{\tau},L\Bigg) = \sum_{i=1}^{N_r}\sum_{n=k-\lfloor\tau_i\rfloor-2L}^{k-\lfloor\tau_i\rfloor+2L-1} \Re\{\Gamma_i\}b_n R_p\left((k-n)-\tau_i\right), \tag{2.20}$$

$$\tag{2.21}$$

and

$$M_{Q_a}\Bigg(\mathbf{s}(k,\boldsymbol{\tau}),\boldsymbol{\Gamma},\boldsymbol{\tau},L\Bigg) = \sum_{i=1}^{N_r}\sum_{n=k+1-\lfloor\tau_i+\frac{1}{2}\rfloor-2L}^{k-\lfloor\tau_i+\frac{1}{2}\rfloor+2L} \Im\{\Gamma_i\}a_n R_p\left(\left(k-n+\frac{1}{2}\right)-\tau_i\right). \tag{2.22}$$

In these equations, M_{Ia} and M_{Ib} are the contributions to the I-branch matched filter output by the multipath components $\Re\{\mathbf{s}(k,\boldsymbol{\tau})\}$ and $\Im\{\mathbf{s}(k,\boldsymbol{\tau})\}$, respectively. Similarly, M_{Qa}, M_{Qb} are the contributions to the Q-branch matched filter output by the multipath components $\Re\{\mathbf{s}(k,\boldsymbol{\tau})\}$ and $\Im\{\mathbf{s}(k,\boldsymbol{\tau})\}$, respectively. An interesting property of the four multipath equations above is that they are all the odd functions of $\mathbf{s}(k,\boldsymbol{\tau})$.

Using standard techniques for error rate analysis, the probability of error can be derived for a given channel multipath fading parameters (Γ_i, τ_i) and a given symbol sequence. The conditional probability that the detector makes a correct decision given $a_k = 1$ and $b_k = 1$ is

$$\Pr(C \mid (a_k,b_k)=(1,1)) = \Pr\{x(k)>0\}\Pr\left\{y\left(k+\frac{1}{2}\right)>0\right\}. \tag{2.23}$$

Substituting (2.13) and (2.15) into the above, we have

$$\begin{aligned}
&\Pr(C \mid (a_k, b_k) = (1,1)) \\
&= \Pr\{a_k + M_{Ia} + M_{Ib} + v_I > 0\}\Pr\{b_k + M_{Qa} + M_{Qb} + v_Q > 0\} \\
&= \Pr\{v_I > -(a_k + M_{Ia} + M_{Ib})\}\Pr\{v_Q > -(b_k + M_{Qa} + M_{Qb}\} \\
&= \{1 - \Pr(v_I > a_k + M_{Ia} + M_{Ib})\}\{1 - \Pr(v_Q > b_k + M_{Qa} + M_{Qb})\} \qquad (2.24)
\end{aligned}$$

where the arguments of the expressions for M_{Ia}, M_{Ib}, M_{Qa}, and M_{Qb} have been omitted for clarity.

Since the noise variable $v \sim CN(0, N_0)$, v_I and v_Q are independent Gaussian random variables with zero mean and $\frac{N_0}{2}$ variance. Applying the Gaussian tail function $Q(\cdot)$, the probability of correct detection is

$$\begin{aligned}
\Pr(C \mid (a_k, b_k) = (1,1)) = &\left[1 - Q\left(\frac{\sqrt{E/2} + M_{Ia} + M_{Ib}}{\sqrt{N_0/2}}\right)\right] \\
&\cdot \left[1 - Q\left(\frac{\sqrt{E/2} + M_{Qa} + M_{Qb}}{\sqrt{N_0/2}}\right)\right]
\end{aligned} \qquad (2.25)$$

where E is the OQPSK symbol energy. If all the symbols and multipath components are normalized, then

$$\begin{aligned}
\Pr(C \mid (a_k, b_k) = (1,1)) = &\left[1 - Q\left(\sqrt{\frac{E}{N_0}}\,(1 + M_{Ia} + M_{Ib})\right)\right] \\
&\cdot \left[1 - Q\left(\sqrt{\frac{E}{N_0}}\,(1 + M_{Qa} + M_{Qb})\right)\right].
\end{aligned} \qquad (2.26)$$

Note that the product of two Guassian tail functions is often tiny, so the conditional probability that the detector makes an incorrect decision given $(a_k, b_k) = (1,1)$ is

$$\begin{aligned}
&\Pr(E \mid (a_k, b_k) = (1,1)) = 1 - \Pr(C \mid (a_k, b_k) = (1,1)) \\
&\qquad \approx Q\left(\sqrt{\frac{E}{N_0}}\,(1 + M_{Ia} + M_{Ib})\right) + Q\left(\sqrt{\frac{E}{N_0}}\,(1 + M_{Qa} + M_{Qb})\right). \qquad (2.27)
\end{aligned}$$

Also note that $E = 2E_b$ and the BER $P_b = \frac{1}{2}\Pr(E)$, thus P_b is

$$P_b(E \mid (a_k, b_k) = (1,1)) = \frac{1}{2}Q\left(\sqrt{\frac{2E_b}{N_0}}\,(1 + M_{Ia} + M_{Ib})\right) + \frac{1}{2}Q\left(\sqrt{\frac{2E_b}{N_0}}\,(1 + M_{Qa} + M_{Qb})\right). \tag{2.28}$$

So the conditional probability of $P_b(E \mid (a_k, b_k))$ is

$$\begin{aligned} P_b(E \mid (a_k, b_k)) = {} & \frac{1}{2}Q\left(\sqrt{\frac{2E_b}{N_0}}\,(1 + M_{Ia}(\mathbf{s}(k,\boldsymbol{\tau}), \mathbf{\Gamma}, \boldsymbol{\tau}, L) + M_{Ib}(\mathbf{s}(k,\boldsymbol{\tau}), \mathbf{\Gamma}, \boldsymbol{\tau}, L)\right) \\ & + \frac{1}{2}Q\left(\sqrt{\frac{2E_b}{N_0}}\,(1 + M_{Qa}(\mathbf{s}(k,\boldsymbol{\tau}), \mathbf{\Gamma}, \boldsymbol{\tau}, L) + M_{Qb}(\mathbf{s}(k,\boldsymbol{\tau}), \mathbf{\Gamma}, \boldsymbol{\tau}, L)\right). \end{aligned} \tag{2.29}$$

Now let us consider the average BER. The matched filter outputs in the I branch M_{Ia}, M_{Ib} are functions of the vectors of $\{\mathbf{s}(k,\boldsymbol{\tau})\}$ which means the set of all possible values of the vectors. The average BER can be directly calculated by the number of these vectors. Let $|\cdot|$ be the number of elements of a set. Then all the possibilities of symbol permutation is $|\{\mathbf{s}(k,\boldsymbol{\tau})\}|$, the average BER can be denoted by

$$\begin{aligned} \bar{P}_b = {} & \frac{1}{|\{\mathbf{s}(k,\boldsymbol{\tau})\}|}\sum_{\{\mathbf{s}(k,\boldsymbol{\tau})\}}\left[\frac{1}{2}Q\left(\sqrt{\frac{2E_b}{N_0}}\,(1 + M_{Ia}(\mathbf{s}(k,\boldsymbol{\tau}), \mathbf{\Gamma}, \boldsymbol{\tau}, L) + M_{Ib}(\mathbf{s}(k,\boldsymbol{\tau}), \mathbf{\Gamma}, \boldsymbol{\tau}, L)\right)\right. \\ & \left. + \frac{1}{2}Q\left(\sqrt{\frac{2E_b}{N_0}}\,(1 + M_{Qa}(\mathbf{s}(k,\boldsymbol{\tau}), \mathbf{\Gamma}, \boldsymbol{\tau}, L) + M_{Qb}(\mathbf{s}(k,\boldsymbol{\tau}), \mathbf{\Gamma}, \boldsymbol{\tau}, L)\right)\right]. \end{aligned} \tag{2.30}$$

2.2 Simulations

The aeronautical telemetry channel is characterized by a complex valued impulse response of the form (2.2) with $N_r = 2$. The first ray is the line-of-sight component, the second ray is a specular reflection characterized by a large amplitude and small delay, and the third ray is a diffuse multipath component characterized by a small amplitude and large delay. To compare the impact of the multipath parameters, four cases of different combinations of $(\Gamma 1, \Gamma 2, \tau 1, \tau 2)$ are chosen as shown

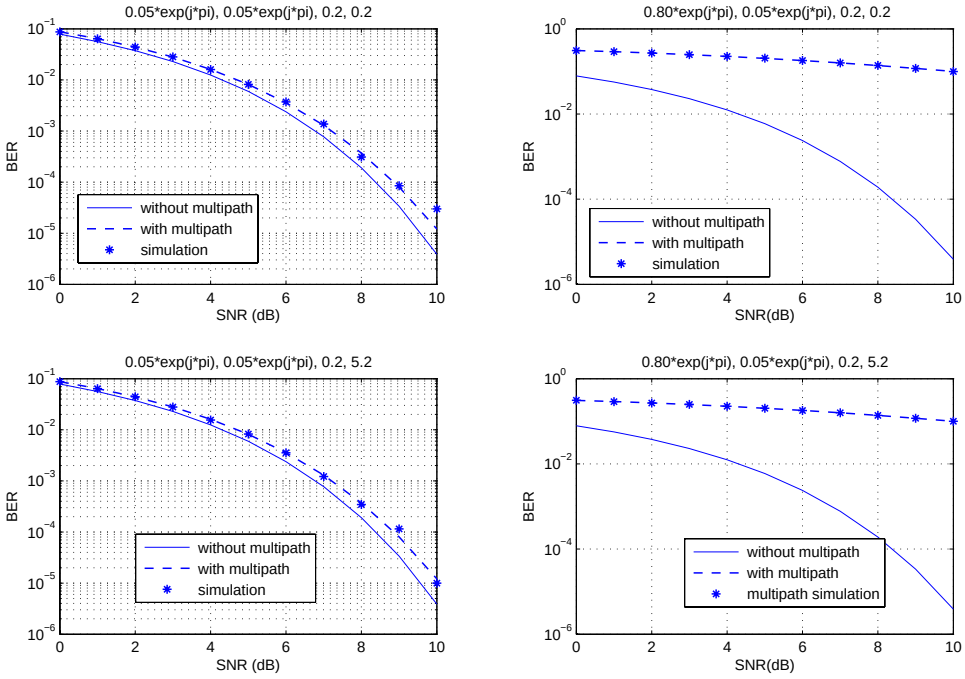

Figure 2.2: Calculated and simulated BER performance for OQPSK with an NRZ pulse shape for three-ray multipath channels.

in the titles of the four subplots. Theoretical calculation of BER with and without multipath rays are given in Figure 2. It can also be seen that the simulations of multipath cases match well with the calculation of the derived multipath equation. To simplify our calculation, the None Return Zero(NRZ) pulse shape is used. This gives $L = 0.5$.

It can be shown from the left two subplots that a multipath ray with a small amplitude and a large delay has an extra $0.5dB$ requirement to obtain the same $BER = 10^{-4}$ as the OQPSK no multipath case. The case $(0.05e^{j\pi}, 0.05e^{j\pi}, 0.2, 4.2)$ has a little bit better performance compared with the case of $(0.05e^{j\pi}, 0.05e^{j\pi}, 0.2, 0.2)$.

From the right two subplots, it can be concluded that a multipath ray with a large amplitude and small delay plays a more dramatical role in the degradation of the BER performance. And the multipath effect is so dominant that the increase of the SNR from $0dB$ to $10dB$ only makes a small improvement in BER and the delay, whether big or small, does not change the BER performance too much.

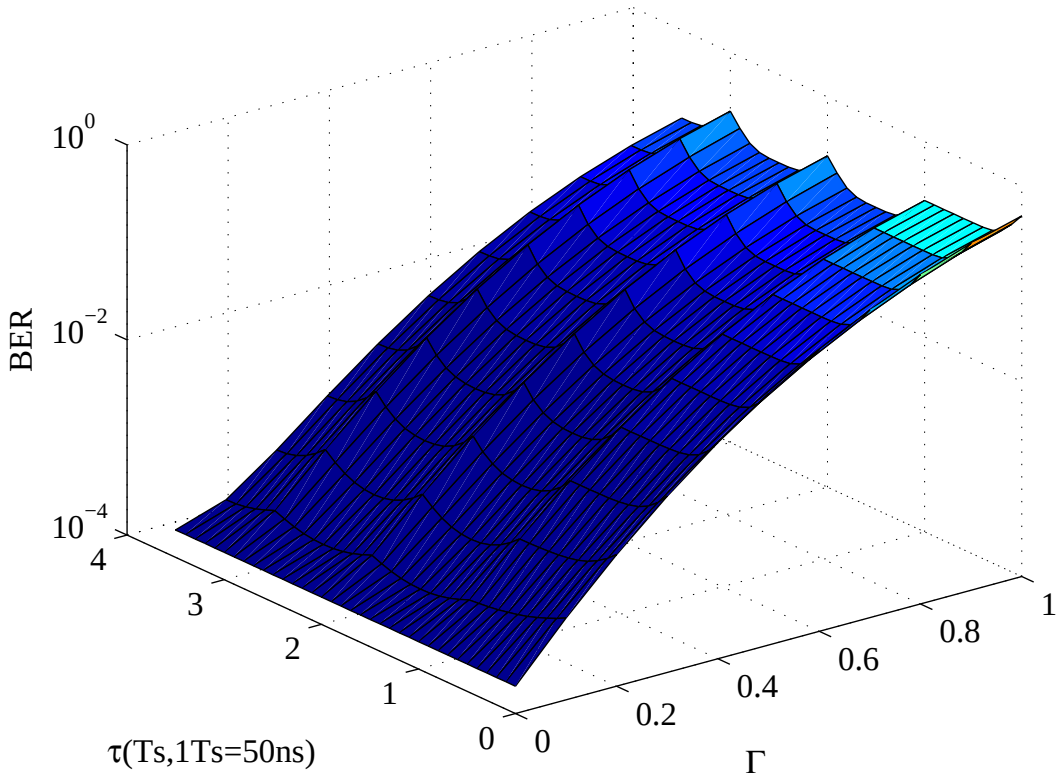

Figure 2.3: BER versus (Γ, τ) pair for SNR = 8 dB.

Further, to completely investigate the relationship of BER versus the multipath parameter pair (Γ, τ) a 3-dimensional plot is given at SNR = 8 dB as shown in Figure 3. Here only one multipath ray is assumed. As we can see from the plot that the BER has a quasi-periodic property with the change of τ, and the BER gets worse with the increase of Γ. This demonstrates that the multipath component with a large Γ with a small τ causes more degradation than the multipath component with small Γ and large τ. From the contour plotting of Figure 4, we can also find the quasi-periodic property of the BER curve for $\tau > Ts$. For a given Gamma, the BER obtains the worst point shortly after half the symbol time.

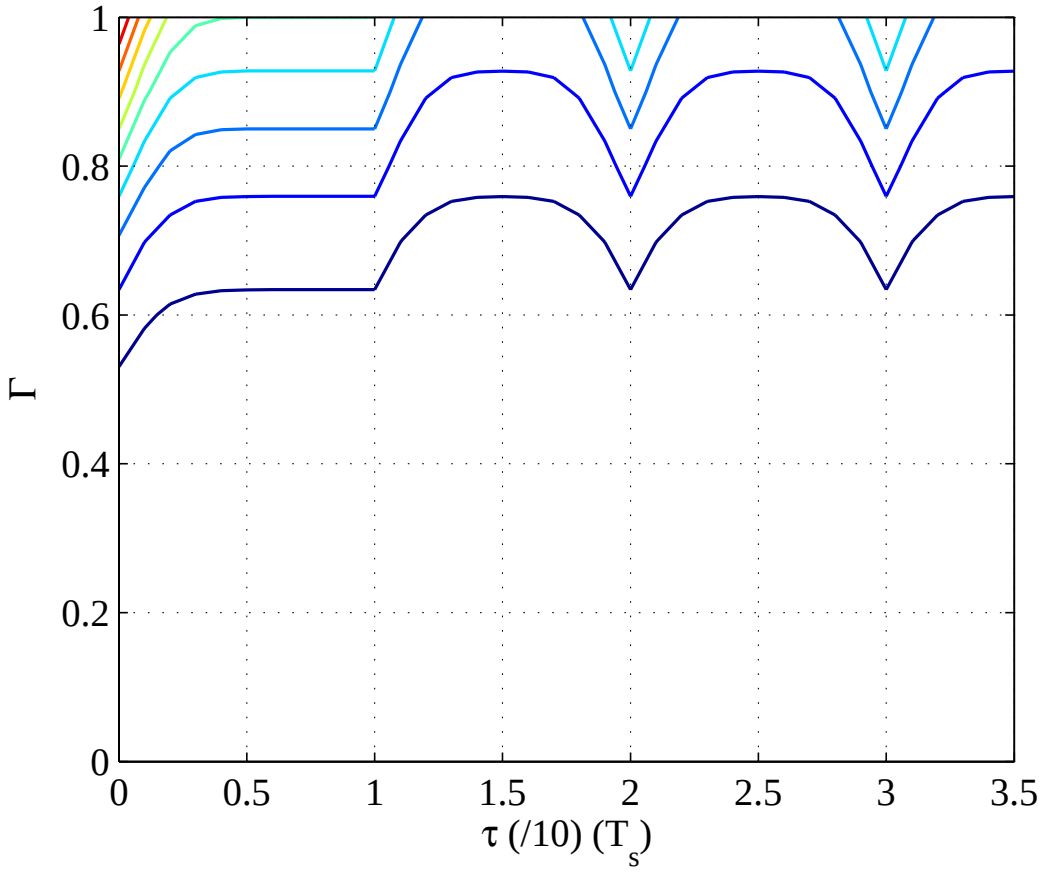

Figure 2.4: Contour of BER versus (Γ, τ) pair for SNR = 8 dB.

2.3 Conclusions

OQPSK BER expressions over the aeronautical telemetry multipath channel have been derived. Simulations show that for the case of a single multipath ray, the BER gets worse with increasing Γ for a fixed delay, and that the BER has a quasi-periodic property for fixed Γ and increasing τ. For the case of two multipath rays, the multipath component characterized by large amplitude and small delay is the main factor of the BER degradation, while the BER is not very sensitive to the change of multipath delay.

Chapter 3

Error Performance of ARTM Tier-1 Waveforms

PCM/FM has been the primary modulation format used in aeronautical telemetry for more than 40 years. During this time, the complexity of the systems that need to be tested has increased dramatically. As a consequence the required data rates for the tests have increased from 100 kbits/sec in the early 1970s to 10-20 Mbit/sec today. This increase has applied tremendous pressure on the spectrum allocated to aeronautical telemetry at L-band (1435 – 1535 MHz), lower S-band (2200 – 2290 MHz), and upper S-band (2310 – 2390 MHz). The situation was further exacerbated in 1997 when the lower portion of upper S-band from 2310 to 2360 MHz was reallocated in two separate auctions[1].

In response to these trends, the Advanced Range Telemetry (ARTM) program [33] was launched by the Central Test and Evaluation Investment Program (CTEIP) in 1997 to identify more bandwidth efficient modulation formats compatible with fully saturated non-linear amplifiers for use in aeronautical telemetry. Modulation formats with improved spectral efficiency were selected in two phases. In the first phase, Feher-patented QPSK (FQPSK) [6] and a compatible variant of the MIL-STD 188-181 Shaped Offset QPSK (SOQPSK) [7] were selected. These two modulation formats, known collectively as "ARTM Tier-1 Waveforms," have twice the spectral efficiency as PCM/FM [8], even when used with non-linear power amplifiers.

As the data rates used for aeronautical telemetry have increased, the multipath interference has become increasingly frequency selective and has proven to be the dominant channel impairment. A model for the multipath in aeronautical telemetry is described in [9] where it was shown that the dominant feature is a "ground

[1] 2320 – 2345 MHz was reallocated for digital audio radio in one auction while 2305 – 2320 MHz and 2345 – 2360 MHz were allocated to wireless communications services in the other auction.

bounce" with complex gain Γ_1 and delay τ_1. The effect of frequency selective multipath interference on PCM/FM was analyzed [13] where it was shown that the loss in bit error rate performance (relative to the AWGN-only environment) is bounded by $(1-|\Gamma_1|)^{-2|\Gamma_1|}$.

In this chapter, we analyze the effect of frequency selective multipath on the ARTM Tier-1 waveforms. We show that in the presence of a strong specular multipath reflection with magnitude $|\Gamma_1|$, the loss in performance for FQPSK is $(1-|\Gamma_1|)^{-4\sqrt{|\Gamma_1|}}$ for $|\Gamma_1| < 0.5$. An error floor at approximately 10^{-2} occurs for $|\Gamma_1| \geq 0.5$. A performance analysis of FQPSK is outlined in Section 3.1 and numerical results are presented in Section 3.2. The relationship between FQPSK and SOQPSK is discussed briefly in Section 3.3. Conclusions are presented in Section 3.4.

3.1 Performance Analysis

3.1.1 Mathematical Description of FQPSK

Feher-patented QPSK (FQPSK) [14] is a variant of offset QPSK where the inphase and quadrature components of the modulated waveform are cross correlated to produce a quasi-constant envelope signal [34, 35]. Following Simon [35], the FQPSK waveform may be expressed in terms of a set of 16 baseband pulse shapes $S_m(t)$ for $m = 0, 1, \ldots, 15$. During the symbol interval $nT_s \leq t \leq (n+1)T_s$, the waveform $S_{i(n)}(t - nT_s)$ is used to amplitude modulate the inphase component of the carrier. Likewise, during the interval $(n+1/2)T_s \leq t \leq (n+3/2)T_s$, the waveform $S_{q(n)}(t - (n-1/2)T_s)$ is used to amplitude modulate the quadrature component of the carrier. The indices $i(n), q(n) \in \{0, 1, \ldots, 15\}$ are determined by the input data streams as described in [35]. The complex baseband FQPSK waveform may be represented as

$$f(t) = \sqrt{E_b} \sum_n \Big[S_{i(n)}(t - nT_s) + jS_{q(n)}(t - (n+1/2)T_s) \Big] \tag{3.1}$$

where E_b is the average bit energy and T_s is the symbol period (or reciprocal of the symbol rate).

3.1.2 Mathematical Analysis

We assume the FQPSK waveform is transmitted over the aeronautical telemetry channel [9] whose impulse response is

$$h(t) = \delta(t) + \Gamma_1\delta(t-\tau_1) + \Gamma_2\delta(t-\tau_2). \tag{3.2}$$

The second and third terms on the right-hand side of (3.2) represent two multipath reflections with complex amplitudes $\Gamma_1 = \Gamma_{1I} + j\Gamma_{1Q}$ and $\Gamma_2 = \Gamma_{2I} + j\Gamma_{2Q}$ and delays τ_1 and τ_2, respectively, as described in [9].

When the FQPSK waveform (3.1) is transmitted through the channel (3.2), the received signal may be represented as

$$r(t) = f(t) * h(t) + w(t) \tag{3.3}$$

$$= f(t) + \Gamma_1 f(t-\tau_1) + \Gamma_2 f(t-\tau_2) + w(t) \tag{3.4}$$

where $w(t) = w_I(t) + jw_Q(t)$ represents the additive thermal noise which is modeled as a complex-valued Gaussian random process where the real and imaginary processes each have zero mean and power spectral densities $N_0/2$ W/Hz.

The optimal detector is a sequence detector using a trellis that accounts for the possible combinations of waveforms determined by the memory of the waveform mapper [35]. In practice, symbol-by-symbol detection is used since this type of detector is compatible with generic offset QPSK and shaped-offset QPSK [5]. The symbol-by-symbol detector is illustrated in Figure 3.1. After rotation by the carrier phase synchronizer, the received waveform is filtered by a detection filter with impulse response $g(t)$ that is normalized to unit energy (i.e. $\int_{-\infty}^{\infty} |g(t)|^2 dt = 1$). Integrate-and-dump detection is realized when

$$g(t) = \begin{cases} \sqrt{\frac{1}{T_s}} & 0 \le t \le T_s \\ 0 & \text{otherwise} \end{cases}. \tag{3.5}$$

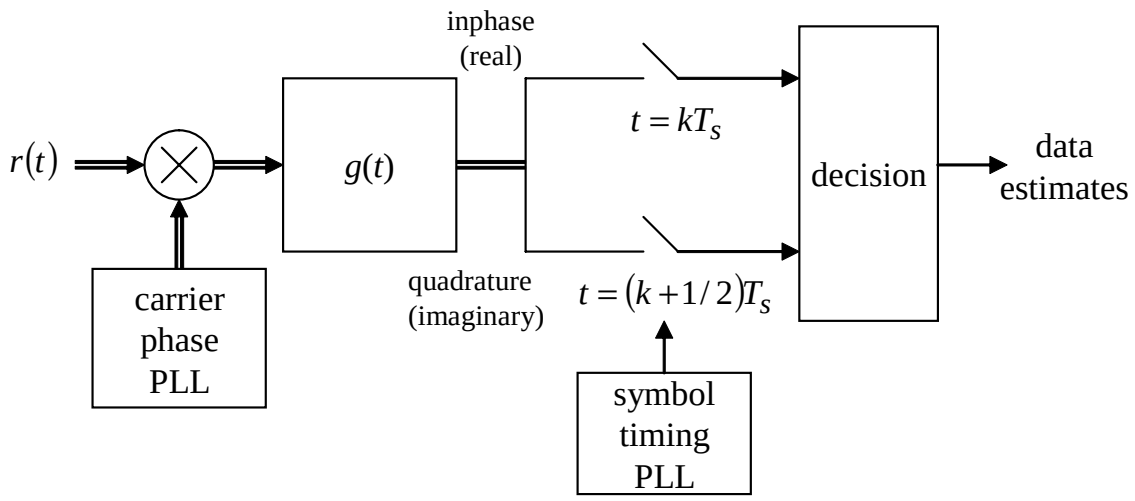

Figure 3.1: Symbol-by-symbol detector for FQPSK and SOQPSK using a simple detection filter.

Simon [35] showed that use of a detection filter matched to the average of the 16 possible waveforms is approximately 1/2 dB better than the integrate-and-dump detection filter in the AWGN environment. (The trellis detector is about 1 dB better than the symbol-by-symbol detector using a detection filter matched to the average of the pulse shapes.)

The complex output of the detection filter is $Z(t) = Z_I(t) + jZ_Q(t)$. The real part of the filter output is sampled at $t = kT_s$ and the imaginary part of the detection filter is sampled at $t = (k+1/2)T_s$ to form an ordered pair which is used for detection.

Let

$$R_m(t) = \int_{-\infty}^{\infty} S_m(x)g(t-x)dx \tag{3.6}$$

be the response of the detection filter to the pulse shape $S_m(t)$ for $m = 0, 1, \ldots, 15$ and

$$v_I(t) = \int_{-\infty}^{\infty} w_I(x)g(t-nT_s-x)dx \tag{3.7}$$

be the detection filter output due to the inphase noise component, then the inphase component of the detection filter output may be expressed as

$$\begin{aligned} Z_I(t) = \sqrt{E_b} \sum_n \Big[& R_{i(n)}(t - nT_s) \\ & + \Gamma_{1I} R_{i(n)}(t - nT_s - \tau_1) \\ & + \Gamma_{2I} R_{i(n)}(t - nT_s - \tau_2) \\ & - \Gamma_{1Q} R_{q(n)}(t - (n + 1/2)T_s - \tau_1) \\ & - \Gamma_{2Q} R_{q(n)}(t - (n + 1/2)T_s - \tau_2) \Big] + v_I(t). \end{aligned} \tag{3.8}$$

The sample at $t = kT_s$ is

$$\begin{aligned} Z_I(kT_s) = \sqrt{E_b} \sum_n \Big[& R_{i(n)}((k - n)T_s) \\ & + \Gamma_{1I} R_{i(n)}((k - n)T_s - \tau_1) \\ & + \Gamma_{2I} R_{i(n)}((k - n)T_s - \tau_2) \\ & - \Gamma_{1Q} R_{q(n)}((k - n - 1/2)T_s - \tau_1) \\ & - \Gamma_{2Q} R_{q(n)}((k - n - 1/2)T_s - \tau_2) \Big] + v_I(kT_s) \end{aligned} \tag{3.9}$$

where $v_I(kT_s)$ is a Gaussian random variable with zero mean and variance $N_0/2$. When the impulse response of the detection filter is zero outside the interval $0 \leq t \leq$

T_s, Equation (3.9) becomes

$$
\begin{aligned}
Z_I(kT_s) = \sqrt{E_b}\Bigg[& R_{i(k)}(0) \\
& + \sum_{n\neq k}\Big\{\Gamma_{1I}R_{i(n)}((k-n)T_s-\tau_1) \\
& + \Gamma_{2I}R_{i(n)}((k-n)T_s-\tau_2) \\
& - \Gamma_{1Q}R_{q(n)}((k-n-1/2)T_s-\tau_1) \\
& - \Gamma_{2Q}R_{q(n)}((k-n-1/2)T_s-\tau_2)\Big\}\Bigg] + v_I(kT_s). \qquad (3.10)
\end{aligned}
$$

The first term on the right-hand side of (3.10) is the decision variable used for detection in the case of no multipath and additive white Gaussian noise. The next four terms (in the summation) represent interference due to the two multipath reflections. The first two of these four terms represent attenuated and delayed versions of the inphase component. The remaining two terms represent attenuated and delayed versions of the quadrature component. We observe that the phase shifts imposed on the delayed signal components cross-couple the inphase and quadrature components of the transmitted signal.

Following the same procedure, the quadrature component of the detection filter output $Z_Q(t)$ and its value at $t = (k+1/2)T_s$ are given by

$$
\begin{aligned}
Z_Q(t) = \sqrt{E_b}\sum_n \Big[& R_{q(n)}(t-(n+1/2)T_s) \\
& + \Gamma_{1I}R_{q(n)}(t-(n+1/2)T_s-\tau_1) \\
& + \Gamma_{2I}R_{q(n)}(t-(n+1/2)T_s-\tau_2) \\
& + \Gamma_{1Q}R_{i(n)}(t-nT_s-\tau_1) \\
& + \Gamma_{2Q}R_{i(n)}(t-nT_s-\tau_2)\Big] + v_Q(t). \qquad (3.11)
\end{aligned}
$$

Similarly, after the sampling, we have

$$
\begin{aligned}
Z_Q((k+1/2)T_s) = \sqrt{E_b}\Bigg[& R_{q(k)}(0) \\
& + \sum_{n\neq k}\Big\{\Gamma_{1I} R_{q(n)}((k-n)T_s - \tau_1) \\
& + \Gamma_{2I} R_{q(n)}((k-n)T_s - \tau_2) \\
& + \Gamma_{1Q} R_{i(n)}((k-n+1/2)T_s - \tau_1) \\
& + \Gamma_{2Q} R_{i(n)}((k-n+1/2)T_s - \tau_2)\Big\}\Bigg] + v_Q((k+1/2)T_s)
\end{aligned} \tag{3.12}
$$

where

$$
v_Q(t) = \int_{-\infty}^{\infty} w_Q(x) g(t - nT_s - x)dx. \tag{3.13}
$$

Again, it has been assumed that the impulse response of the detection filter is zero outside the interval $0 \leq t \leq T_s$. $v_Q((k+1/2)T_s)$ is a Gaussian random variable with zero mean and variance $N_0/2$ that and is independent of $v_I(kT_s)$.

For notational simplicity, the expressions (3.10) and (3.12) can be expressed as

$$
Z_I(kT_s) = \sqrt{E_b} R_{i(k)}(0) + M_I(k) + v_I(kT_s) \tag{3.14}
$$

and

$$
Z_Q((k+1/2)T_s) = \sqrt{E_b} R_{q(k)}(0) + M_Q(k) + v_Q((k+1/2)T_s). \tag{3.15}
$$

The terms of $M_I(k), M_Q(k)$ quantify the distortion of the multipath interference normalized to the average symbol energy. In reality, $M_I(k)$ and $M_Q(k)$ are functions not only of the time index k, but also the waveforms $S_{i(n)}$ and $S_{q(n)}$ and the multipath parameters Γ_1, τ_1, Γ_2, and τ_2. The dependence is not explicit since to make it so is notationally cumbersome. They can be defined as

$$M_I(k) = \sqrt{E_b} \sum_{n \neq k} \Big\{ \Gamma_{1I} R_{i(n)}((k-n)T_s - \tau_1) + \Gamma_{2I} R_{i(n)}((k-n)T_s - \tau_2) - \Gamma_{1Q} R_{q(n)}((k-n-1/2)T_s - \tau_1) - \Gamma_{2Q} R_{q(n)}((k-n-1/2)T_s - \tau_2) \Big\} \tag{3.16}$$

and

$$M_Q(k) = \sqrt{E_b} \sum_{n \neq k} \Big\{ \Gamma_{1I} R_{q(n)}((k-n)T_s - \tau_1) + \Gamma_{2I} R_{q(n)}((k-n)T_s - \tau_2) + \Gamma_{1Q} R_{i(n)}((k-n+1/2)T_s - \tau_1) + \Gamma_{2Q} R_{i(n)}((k-n+1/2)T_s - \tau_2) \Big\}. \tag{3.17}$$

For a given pair of waveforms $S_{i(k)}$ and $S_{q(k)}$ the probability of bit error, $P(b|i(k), q(k))$, can be obtained using standard analysis techniques [36] and may be expressed as

$$P(b|i(k), q(k)) = \frac{1}{2} Q\left(\sqrt{\frac{2E_b}{N_0} \left[R_{i(k)}(0) + M_I(k) \right]^2} \right) + \frac{1}{2} Q\left(\sqrt{\frac{2E_b}{N_0} \left[R_{q(k)}(0) + M_Q(k) \right]^2} \right). \tag{3.18}$$

The average probability of error is obtained from (3.18) by averaging over the possible values for $M_I(k)$ and $M_Q(k)$ for each possible symbol index pair $i(k)$ and $q(k)$.

3.2 Numerical Results

The bit error rate is a function of the multipath parameters Γ_1, τ_1, Γ_2, and τ_2. These parameters vary with time as the air-borne transmitter progresses along its flight path. Average values of these parameters, reported in [9], are:

$$|\Gamma_1| = 0.85 \qquad \tau_1 = 45 \text{ nsec} \tag{3.19}$$

$$|\Gamma_2| = 0.01 \qquad \tau_2 = 155 \text{ nsec} \tag{3.20}$$

The first multipath propagation path is characterized by a large amplitude and short delay. This component models a strong "ground bounce" that is a common occurrence at test ranges in the Western USA. The second multipath reflection is characterized by a small amplitude and larger delay. This component is a diffuse component with random variations as described in [9].

The number of non-zero terms in the normalized multipath components $M_I(k)$ and $M_Q(k)$ are determined by the relationship between τ_1, τ_2 and the symbol interval T_s. Since the symbol interval T_s is the reciprocal of the symbol rate, the way the multipath interference effects the bit error rate performance is a function of the symbol rate. For low bit rates, T_s is large relative to τ_1 and τ_2 and the multipath interference manifests itself as frequency non-selective (or "flat") fading [36, Chapter 13]. At higher bit rates, T_s is on the order of τ_1 and τ_2 and the multipath interference produces a frequency selective fading processes [36, Chapter 13].

The bit rates of practical interest to aeronautical telemetry are 5, 10, and 20 Mbits/sec. The relationship between these bit rates and the multipath delays τ_1 and τ_2 is summarized in Table 3.1. For 10 Mbits/sec, the longest multipath delay is less than a symbol time (but greater than 1/2 the symbol time). Thus, the multipath introduces intersymbol interference from the proceeding two symbols. In this case,

the normalized multipath components are given by

$$M_I(k) = \sqrt{E_b}\Bigg[\Gamma_{1I}R_{i(k-1)}(T_s-\tau_1)+\Gamma_{1I}R_{i(k)}(-\tau_1) - \Gamma_{1Q}R_{q(k-1)}\left(\frac{T_s}{2}-\tau_1\right)-\Gamma_{1Q}R_{q(k)}\left(-\frac{T_s}{2}-\tau_1\right) + \Gamma_{2I}R_{i(k-1)}(T_s-\tau_2)+\Gamma_{2I}R_{i(k)}(-\tau_2) -\Gamma_{2Q}R_{q(k-2)}\left(\frac{3T_s}{2}-\tau_2\right)-\Gamma_{2Q}R_{q(k-1)}\left(\frac{T_s}{2}-\tau_2\right)\Bigg] \quad (3.21)$$

and

$$M_Q(k) = \sqrt{E_b}\Bigg[\Gamma_{1I}R_{q(k-1)}(T_s-\tau_1)+\Gamma_{1I}R_{q(k)}(-\tau_1) + \Gamma_{1Q}R_{i(k)}\left(\frac{T_s}{2}-\tau_1\right)+\Gamma_{1Q}R_{i(k+1)}\left(-\frac{T_s}{2}-\tau_1\right) + \Gamma_{2I}R_{q(k-1)}(T_s-\tau_2)+\Gamma_{2I}R_{q(k)}(-\tau_2) +\Gamma_{2Q}R_{i(k-1)}\left(\frac{3T_s}{2}-\tau_2\right)+\Gamma_{2Q}R_{i(k)}\left(\frac{T_s}{2}-\tau_2\right)\Bigg]. \quad (3.22)$$

When the bit rate is increased to 20 Mbits/sec, the longest multipath delay is approximately one and one-half times the symbol interval. The multipath interference introduces intersymbol interference from the preceding three symbols so that the normalized multipath components are given by

$$M_I(k) = \sqrt{E_b}\Bigg[\Gamma_{1I}R_{i(k-1)}(T_s-\tau_1)+\Gamma_{1I}R_{i(k)}(-\tau_1) - \Gamma_{1Q}R_{q(k-1)}\left(\frac{T_s}{2}-\tau_1\right)-\Gamma_{1Q}R_{q(k)}\left(-\frac{T_s}{2}-\tau_1\right) + \Gamma_{2I}R_{i(k-2)}(2T_s-\tau_2)+\Gamma_{2I}R_{i(k-1)}(T_s-\tau_2) -\Gamma_{2Q}R_{q(k-3)}\left(\frac{5T_s}{2}-\tau_2\right)-\Gamma_{2Q}R_{q(k-2)}\left(\frac{3T_s}{2}-\tau_2\right)\Bigg] \quad (3.23)$$

Table 3.1: The relationship between bit rate and multipath delays τ_1 and τ_2

Bit Rate Mbits/sec	Symbol Rate Msymbols/sec	τ_1/T_s	τ_2/T_s
5.0	2.5	0.1125	0.3875
10.0	5.0	0.225	0.775
20.0	10.0	0.45	1.55

and

$$M_Q(k) = \sqrt{E_b}\Bigg[\Gamma_{1I}R_{q(k-1)}(T_s-\tau_1) + \Gamma_{1I}R_{q(k)}(-\tau_1) + \Gamma_{1Q}R_{i(k)}\left(\frac{T_s}{2}-\tau_1\right) + \Gamma_{1Q}R_{i(k+1)}\left(-\frac{T_s}{2}-\tau_1\right) + \Gamma_{2I}R_{q(k-2)}(2T_s-\tau_2) + \Gamma_{2I}R_{q(k-1)}(T_s-\tau_2) + \Gamma_{2Q}R_{i(k-2)}\left(\frac{5T_s}{2}-\tau_2\right) + \Gamma_{2Q}R_{i(k-1)}\left(\frac{3T_s}{2}-\tau_2\right)\Bigg]. \quad (3.24)$$

The average probability of bit error is obtained from (3.18) by averaging over the possible waveforms. In the presence of multipath, the averaging needs to include the possible waveforms during the preceding two symbol interval (for 5 and 10 Mbits/sec) and the possible waveforms during the three preceding intervals (for 20 Mbits/sec). For a given waveform $S_m(t)$ on the inphase component, there are four possible inphase component waveforms during the preceding interval as summarized in Table 3.2. Similarly, a given waveform on the quadrature component has four possible quadrature component waveforms during the preceding interval as summarized in Table 3.2. Evaluation of (3.21) – (3.24) also requires knowledge of the possible inphase/quadrature pairings for the waveforms as well as the possible waveforms during the preceding interval on the opposite component. This information is listed in Table 3.3 and Table 3.2. For each possibility, the information in Table 3.2 can be used to determine the possible waveforms on the quadrature component during the preceding intervals.

Application of the technique is demonstrated for the 10 Mbit/sec case. Let $\mathcal{K}$ represent the set of all possible waveform indices for $S_{i(k)}(t)$, $S_{q(k)}(t-T_s/2)$, $S_{i(k-1)}(t-$

Table 3.2: FQPSK waveform transitions for either I or Q branch.

Waveform over the interval $kT_s \le t \le (k+1)T_s$	Possible waveforms over the interval $(k-1)T_s \le t \le kT_s$
$S_0(t)$	$S_0(t), S_2(t), S_4(t), S_6(t)$
$S_1(t)$	$S_0(t), S_2(t), S_4(t), S_6(t)$
$S_2(t)$	$S_0(t), S_2(t), S_4(t), S_6(t)$
$S_3(t)$	$S_0(t), S_2(t), S_4(t), S_6(t)$
$S_4(t)$	$S_9(t), S_{11}(t), S_{13}(t), S_{15}(t)$
$S_5(t)$	$S_9(t), S_{11}(t), S_{13}(t), S_{15}(t)$
$S_6(t)$	$S_9(t), S_{11}(t), S_{13}(t), S_{15}(t)$
$S_7(t)$	$S_9(t), S_{11}(t), S_{13}(t), S_{15}(t)$
$S_8(t)$	$S_8(t), S_{10}(t), S_{12}(t), S_{14}(t)$
$S_9(t)$	$S_8(t), S_{10}(t), S_{12}(t), S_{14}(t)$
$S_{10}(t)$	$S_8(t), S_{10}(t), S_{12}(t), S_{14}(t)$
$S_{11}(t)$	$S_8(t), S_{10}(t), S_{12}(t), S_{14}(t)$
$S_{12}(t)$	$S_1(t), S_3(t), S_5(t), S_7(t)$
$S_{13}(t)$	$S_1(t), S_3(t), S_5(t), S_7(t)$
$S_{14}(t)$	$S_1(t), S_3(t), S_5(t), S_7(t)$
$S_{15}(t)$	$S_1(t), S_3(t), S_5(t), S_7(t)$

$T_s)$, $S_{q(k-1)}(t - 3T_s/2)$, $S_{i(k-2)}(t - 2T_s)$, and $S_{q(k-2)}(t - 7T_s/2)$. Averaging over the possibilities yields the average probability of bit error

$$P(b) = \frac{1}{2|\mathcal{K}|} \sum_{k \in \mathcal{K}} \left\{ Q\left(\sqrt{\frac{2E_b}{N_0} \left[R_{i(k)}(0) + M_I(k) \right]^2} \right) + Q\left(\sqrt{\frac{2E_b}{N_0} \left[R_{q(k)}(0) + M_Q(k) \right]^2} \right) \right\}. \tag{3.25}$$

A plot of this expression for 10 Mbit/sec and the corresponding expression for 20 Mbit/sec FQPSK in a multipath channel characterized by $\Gamma_1 = 0.85e^{j\pi/4}$, $\tau_1 = 45$ nsec, $\Gamma_2 = 0.01$, $\tau_2 = 155$ nsec is plotted in Figure 3.2. The performance of FQPSK in the AWGN environment is shown for comparison. Note that the multipath interference causes substantial loss. The loss is much worse when the phase of Γ_1 is π, as shown in Figure 3.3. Simulation results for 10 Mbit/sec FQPSK over this multipath channel are also included and show very close agreement with the analysis.

Table 3.3: FQPSK waveform transitions for inphase and quadrature pair

$(i(n), q(n))$	possible $(i(n-1), q(n-1))$			
$(0,0)$	$(0,0)$	$(2,4)$	$(4,0)$	$(6,4)$
$(0,1)$	$(0,0)$	$(2,4)$	$(4,0)$	$(6,4)$
$(1,2)$	$(0,0)$	$(2,4)$	$(4,0)$	$(6,4)$
$(1,3)$	$(0,0)$	$(2,4)$	$(4,0)$	$(6,4)$
$(2,12)$	$(0,1)$	$(2,5)$	$(4,1)$	$(6,5)$
$(2,13)$	$(0,1)$	$(2,5)$	$(4,1)$	$(6,5)$
$(3,14)$	$(0,1)$	$(2,5)$	$(4,1)$	$(6,5)$
$(3,15)$	$(0,1)$	$(2,5)$	$(4,1)$	$(6,5)$
$(0,8)$	$(2,12)$	$(0,8)$	$(6,12)$	$(4,8)$
$(0,9)$	$(2,12)$	$(0,8)$	$(6,12)$	$(4,8)$
$(1,10)$	$(2,12)$	$(0,8)$	$(6,12)$	$(4,8)$
$(1,11)$	$(2,12)$	$(0,8)$	$(6,12)$	$(4,8)$
$(2,4)$	$(2,13)$	$(0,9)$	$(6,13)$	$(4,9)$
$(2,5)$	$(2,13)$	$(0,9)$	$(6,13)$	$(4,9)$
$(3,6)$	$(2,13)$	$(0,9)$	$(6,13)$	$(4,9)$
$(3,7)$	$(2,13)$	$(0,9)$	$(6,13)$	$(4,9)$
$(4,0)$	$(13,2)$	$(15,6)$	$(9,2)$	$(11,6)$
$(4,1)$	$(13,2)$	$(15,6)$	$(9,2)$	$(11,6)$
$(5,2)$	$(13,2)$	$(15,6)$	$(9,2)$	$(11,6)$
$(5,3)$	$(13,2)$	$(15,6)$	$(9,2)$	$(11,6)$
$(6,12)$	$(13,3)$	$(15,7)$	$(9,3)$	$(11,7)$
$(6,13)$	$(13,3)$	$(15,7)$	$(9,3)$	$(11,7)$
$(7,14)$	$(13,3)$	$(15,7)$	$(9,3)$	$(11,7)$
$(7,15)$	$(13,3)$	$(15,7)$	$(9,3)$	$(11,7)$
$(4,8)$	$(15,14)$	$(13,10)$	$(11,14)$	$(9,10)$
$(4,9)$	$(15,14)$	$(13,10)$	$(11,14)$	$(9,10)$
$(5,10)$	$(15,14)$	$(13,10)$	$(11,14)$	$(9,10)$
$(5,11)$	$(15,14)$	$(13,10)$	$(11,14)$	$(9,10)$
$(6,4)$	$(15,15)$	$(13,11)$	$(11,15)$	$(9,11)$
$(6,5)$	$(15,15)$	$(13,11)$	$(11,15)$	$(9,11)$
$(7,6)$	$(15,15)$	$(13,11)$	$(11,15)$	$(9,11)$
$(7,7)$	$(15,15)$	$(13,11)$	$(11,15)$	$(9,11)$

Table 3.3-Continued

$(i(n), q(n))$	possible $(i(n-1), q(n-1))$			
$(8,0)$	$(12,0)$	$(14,4)$	$(8,0)$	$(10,4)$
$(8,1)$	$(12,0)$	$(14,4)$	$(8,0)$	$(10,4)$
$(9,2)$	$(12,0)$	$(14,4)$	$(8,0)$	$(10,4)$
$(9,3)$	$(12,0)$	$(14,4)$	$(8,0)$	$(10,4)$
$(10,12)$	$(12,1)$	$(14,5)$	$(8,1)$	$(10,5)$
$(10,13)$	$(12,1)$	$(14,5)$	$(8,1)$	$(10,5)$
$(11,14)$	$(12,1)$	$(14,5)$	$(8,1)$	$(10,5)$
$(11,15)$	$(12,1)$	$(14,5)$	$(8,1)$	$(10,5)$
$(8,8)$	$(14,12)$	$(12,8)$	$(10,12)$	$(8,8)$
$(8,9)$	$(14,12)$	$(12,8)$	$(10,12)$	$(8,8)$
$(9,10)$	$(14,12)$	$(12,8)$	$(10,12)$	$(8,8)$
$(9,11)$	$(14,12)$	$(12,8)$	$(10,12)$	$(8,8)$
$(10,4)$	$(14,13)$	$(12,9)$	$(10,13)$	$(8,9)$
$(10,5)$	$(14,13)$	$(12,9)$	$(10,13)$	$(8,9)$
$(11,6)$	$(14,13)$	$(12,9)$	$(10,13)$	$(8,9)$
$(11,7)$	$(14,13)$	$(12,9)$	$(10,13)$	$(8,9)$
$(12,0)$	$(1,2)$	$(3,6)$	$(5,2)$	$(7,6)$
$(12,1)$	$(1,2)$	$(3,6)$	$(5,2)$	$(7,6)$
$(13,2)$	$(1,2)$	$(3,6)$	$(5,2)$	$(7,6)$
$(13,3)$	$(1,2)$	$(3,6)$	$(5,2)$	$(7,6)$
$(14,12)$	$(1,3)$	$(3,7)$	$(5,3)$	$(7,7)$
$(14,13)$	$(1,3)$	$(3,7)$	$(5,3)$	$(7,7)$
$(15,14)$	$(1,3)$	$(3,7)$	$(5,3)$	$(7,7)$
$(15,15)$	$(1,3)$	$(3,7)$	$(5,3)$	$(7,7)$
$(12,8)$	$(3,14)$	$(1,10)$	$(7,14)$	$(5,10)$
$(12,9)$	$(3,14)$	$(1,10)$	$(7,14)$	$(5,10)$
$(13,10)$	$(3,14)$	$(1,10)$	$(7,14)$	$(5,10)$
$(13,11)$	$(3,14)$	$(1,10)$	$(7,14)$	$(5,10)$
$(14,4)$	$(3,15)$	$(1,11)$	$(7,15)$	$(5,11)$
$(14,5)$	$(3,15)$	$(1,11)$	$(7,15)$	$(5,11)$
$(15,6)$	$(3,15)$	$(1,11)$	$(7,15)$	$(5,11)$
$(15,7)$	$(3,15)$	$(1,11)$	$(7,15)$	$(5,11)$

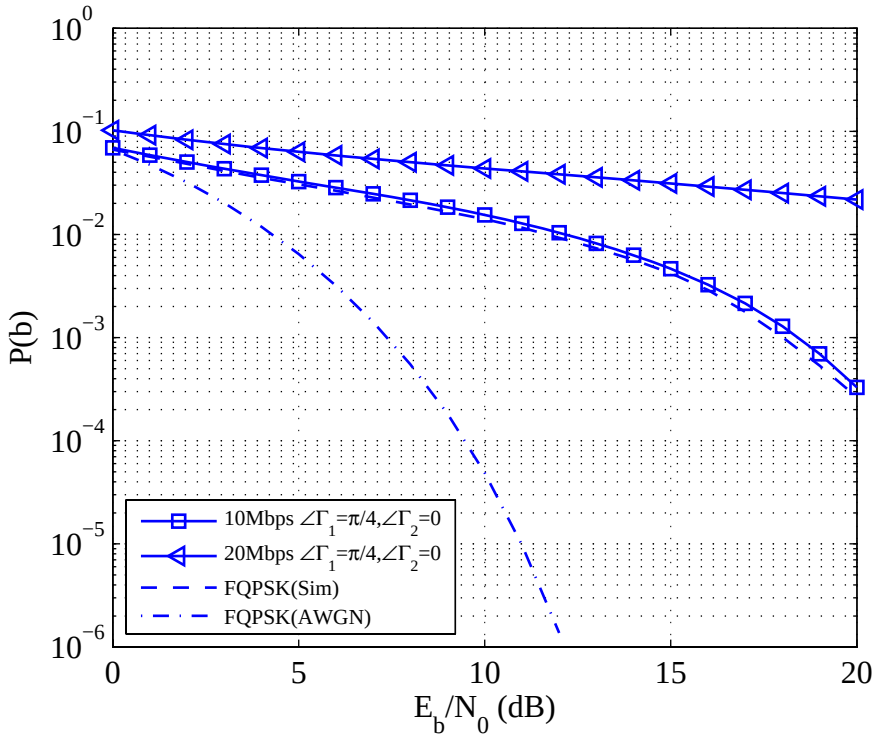

Figure 3.2: Probability of bit error versus E_b/N_0 for 20 Mbit/sec FQPSK and 10 Mbit/sec FQPSK in a multipath fading channel with $\Gamma_1 = 0.85e^{j\pi/4}$, $\tau_1 = 45$ nsec, $\Gamma_2 = 0.01$, $\tau_2 = 155$ nsec. Simulations for 10 Mbit/sec FQPSK in the same channel are also included. The performance of FQPSK in the AWGN environment is shown for comparison.

The effect of a single multipath reflection on the performance of FQPSK can be assessed using (3.25) where (3.21) and (3.22) are evaluated with $\Gamma_{2I} = \Gamma_{2Q} = 0$. Suitable, but straight-forward, alterations are also required when $\tau_1 > T_s$. The results of this analysis are summarized in Figures 3.3 and 3.4. The average probability of bit error (3.25) is evaluated for $\tau_1/T_s = 0.45$ for different values of $|\Gamma_1|$ and different values of $\angle\Gamma_1$ in Figure 3.3. Observe that both $|\Gamma_1|$ and $\angle\Gamma_1$ have a pronounced effect on the behavior of the average bit error probability. When $\angle\Gamma_1 = 0$, the multipath produces constructive interference so that $P(b)$ decreases as $|\Gamma_1|$ increases. In this case, the multipath interference actually improves the bit error probability over the AWGN value. At the other extreme, $\angle\Gamma_1 = \pi$ produces the most destructive interference so that the average bit error probability increases as $|\Gamma_1|$ increases as shown. The dependence on $\angle\Gamma_1$ is emphasized in Figure 3.4. Note that the minima

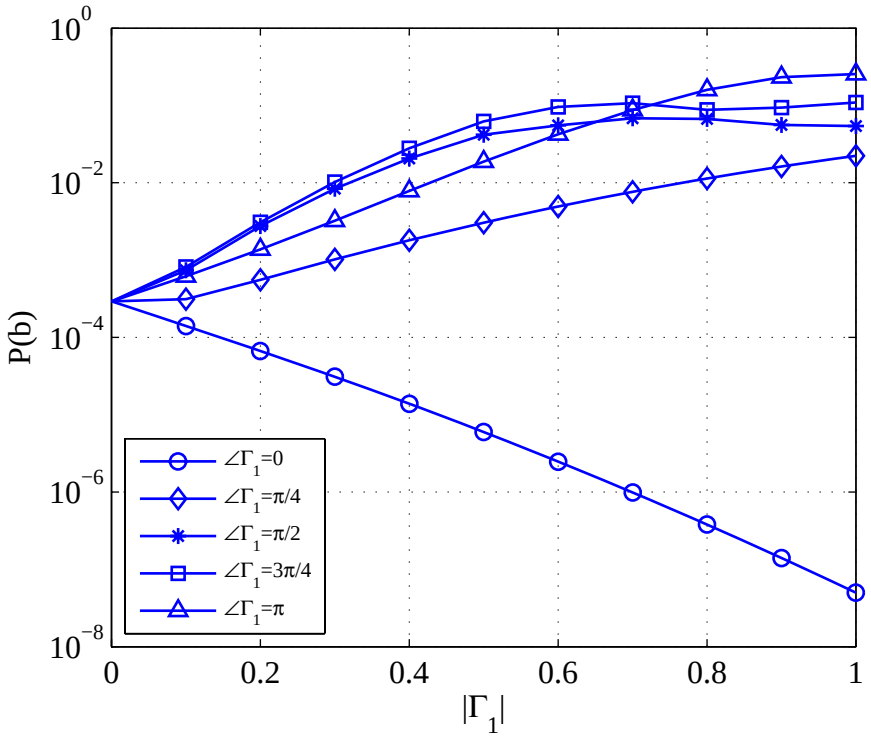

Figure 3.3: Probability of bit error versus $|\Gamma_1|$ for $E_b/N_0 = 10$ dB, $\tau_1/T_s = 0.225$, and various values of $\angle\Gamma_1$.

for each value of Γ_1 occur at $\angle\Gamma_1 = 0$ which corresponds to the case of maximum destructive interference.

The dependence between $P(b)$ and $\angle\Gamma_1$ is to be expected since $\angle\Gamma_1$ is the dominant quantity in determining the location of the spectral null produced by the multipath interference [9]. In real scenarios, $\angle\Gamma_1$ changes with time so that the multipath null appears to "sweep" through the spectrum of the received signal when viewed on a spectrum analyzer in real time.

The probability of bit error averaged over $\phi = \angle\Gamma_1$ is of interest [13]. The average probability of bit error,

$$\overline{P}(b) = \frac{1}{2\pi}\int_{-\pi}^{\pi} P(b,\phi)d\phi \tag{3.26}$$

is plotted in Figure 3.5 for various values of $|\Gamma_1|$. Observe that the loss in performance, relative to the AWGN environment, varies as a function of $|\Gamma_1|$ as summarized in

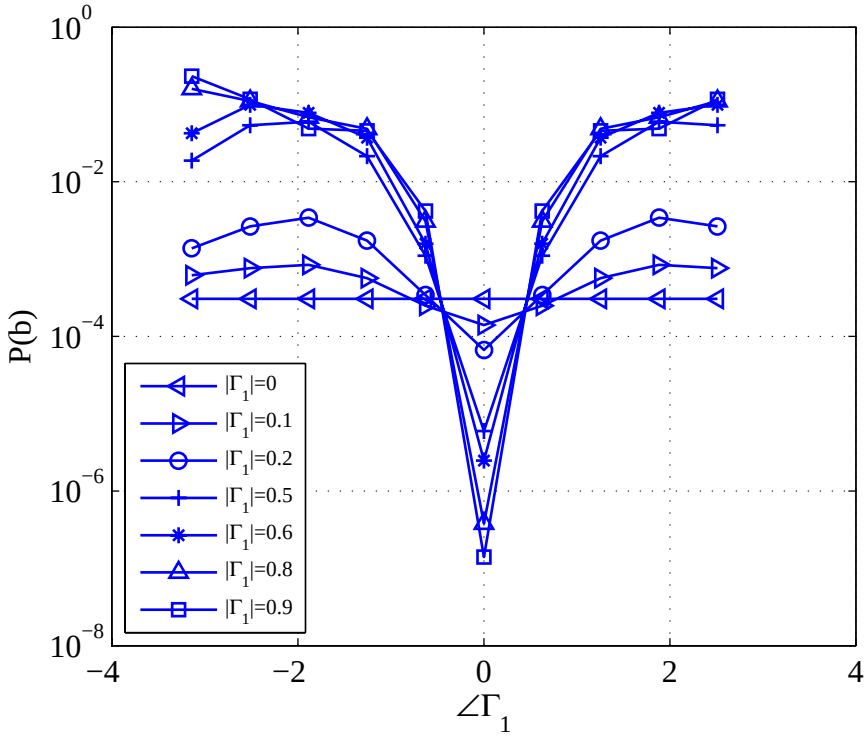

Figure 3.4: Probability of bit error versus $\angle\Gamma_1$ for $E_b/N_0 = 10$ dB, $\tau_1/T_s = 0.225$, and various values of $|\Gamma_1|$.

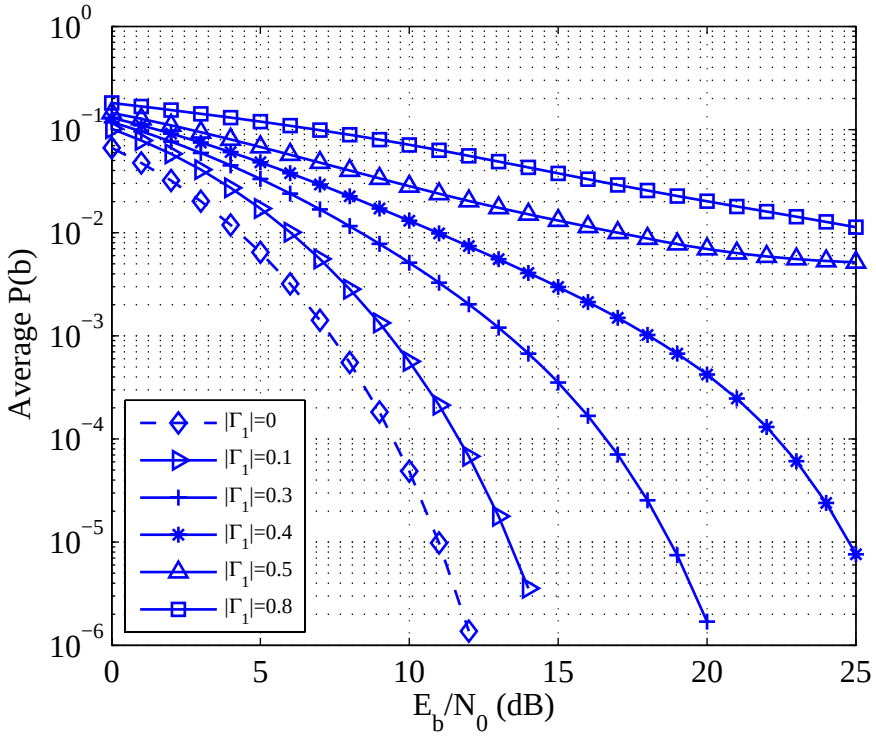

Figure 3.5: The phase averaged probability of bit error $\overline{P}(b)$ versus E_b/N_0 for FQPSK for various values of $|\Gamma_1|$.

Table 3.4: FQPSK Performance multipath loss at $\overline{P}(b) = 10^{-5}$ relative to the AWGN.

$\|\Gamma_1\|$	loss from Figure 3.5 (dB)	loss predicted by (3.27) (dB)
0.0	0	0
0.1	0.99	1.16
0.2	3.10	3.47
0.3	6.40	6.79
0.4	12.40	11.22
0.5	–	–

Table 3.4. The loss in performance is approximately

$$L_{\text{FQPSK}} \approx (1 - |\Gamma_1|)^{-4\sqrt{|\Gamma_1|}} . \tag{3.27}$$

The loss in performance for FQPSK exceeds that for PCM/FM. In addition, Figure 3.5 suggests that the multipath causes an error floor for FQPSK. For the range of signal-to-noise ratios shown, this error floor is observable for $|\Gamma_1| \geq 0.5$. This error floor is much higher than the error floor for PCM/FM.

3.3 The Performance of SOQPSK

Shaped Offset QPSK (SOQPSK) is a ternary CPM modulation format whose modulation index $h = 1/2$. Using complex baseband notation, the SOQPSK waveform may be represented as

$$s(t) = \exp\{j\phi(t)\}, \tag{3.28}$$

and

$$\phi(t) = \pi \sum_k \alpha(k) g(t - kT_b) \tag{3.29}$$

where $\alpha(k) \in \{-1, 0, +1\}$ is the k-th ternary symbol, T_b is the bit time, and $g(t)$ is a phase pulse that is the time integral of a frequency pulse $p(t)$ with area 1/2. The frequency pulse defined in MIL-STD 188-181 is a rectangular pulse with duration T_b and amplitude $T_b/2$. IRIG-106 specifies a more bandwidth efficient variation of this waveform which it terms SOQPSK-TG. The frequency pulse for SOQPSK-TG is a

spectral raised cosine pulse that is been windowed by a *temporal* raised-cosine. The phase and frequency pulses for SOQPSK-TG are given by [7]

$$g(t) = \int_{-\infty}^{t} p(x)dx, \tag{3.30}$$

and

$$p(t) = A\frac{\cos\left(\frac{\pi\rho Bt}{2T_b}\right)}{1-4\left(\frac{\rho Bt}{2T_b}\right)^2} \times \frac{\sin\left(\frac{\pi Bt}{2T_b}\right)}{\frac{\pi Bt}{2T_b}} \times w_n(t) \tag{3.31}$$

where the window is

$$w_n(t) = \begin{cases} 1 & 0 \le \left|\frac{t}{2T_b}\right| \le T_1 \\ \frac{1}{2} + \frac{1}{2}\cos\left(\frac{\pi}{T_2}\left(\frac{t}{2T_b} - T_1\right)\right) & T_1 \le \left|\frac{t}{2T_b}\right| \le T_1 + T_2 \\ 0 & T_1 + T_2 < \left|\frac{t}{2T_b}\right| \end{cases} \tag{3.32}$$

and the constant A is chosen to make the area of $p(t)$ equal to $1/2$. The waveform is completely specified by the parameters ρ, B, T_1, and T_2. For SOQPSK-TG the values are[2] $\rho = 0.7$, $B = 1.25$, $T_1 = 1.5$, and $T_2 = 0.5$. The frequency pulse has support on the interval $-2 \le t/2T_b \le 2$ and thus spans 4 signaling intervals. SOQPSK-TG is an example of *partial response* CPM [37]. The mapping from bits to ternary symbols is described in [7].

The name "shaped offset QPSK" follows from the observation that each ternary symbol causes the carrier phase either advance by $\pm\pi/2$ radians or to remain at its current value. When viewed on an I-Q plot, the carrier phase appears to migrate from quadrant to quadrant along the unit circle. By contrast, the carrier phase of (unshaped) Offset QPSK migrates from quadrant to quadrant instantaneously. Since

[2]In the original publication [7], two versions of SOQPSK were described: SOQPSK-A defined by $\rho = 1$, $B = 1.35$, $T_1 = 1.4$, and $T_2 = 0.6$ and SOQPSK-B defined by $\rho = 0.5$, $B = 1.45$, $T_1 = 2.8$, and $T_2 = 1.2$. SOQPSK-A has a slightly narrower bandwidth (measured at the -60 dB level) and slightly worse detection efficiency than SOQPSK-B. The Telemetry Group of the Range Commanders Council adopted the compromise waveform, designated SOQPSK-TG in 2003.

the phase pulse "shapes" the phase trajectory of the carrier from what it would be for unshaped OQPSK, the waveform has an interpretation as a "shaped" OQPSK.

The use of a linear detector of the form illustrated in Figure 3.1 for use with binary CPM with $h = 1/2$ has been analyzed in [38, 39, 40] and applied in [41, 42]. Detection filters for SOQPSK have been studied by Geoghegan, et. al [16] using experimental techniques.

To date, the performance of a linear detector for *ternary* CPM has not been analyzed. Given the analytical difficulties of evaluating the performance of a ternary non-linear modulation, we resort to simulations to demonstrate that the bit error rate performance of SOQPSK is very close to that of FQPSK. The simulation results for 10 Mbit/sec SOQPSK in the a multipath channel characterized by $\Gamma_1 = 0.85e^{j\pi/4}$, $\tau_1 = 45$ nsec, $\Gamma_2 = 0.01$, $\tau_2 = 155$ nsec and using the detection filter (3.5) is plotted in Figure 3.6. Note the close agreement between the 10 Mbit/sec FQPSK performance curve and the 10 Mbit/sec SOQPSK performance curve. This and other simulation results [16] demonstrate that the conclusions drawn for FQPSK based on the analysis also apply to SOQPSK.

3.4 Conclusions

The bit error rate performance of FQPSK and SOQPSK (collectively known as the ARTM Tier-1 waveforms) was analyzed in a frequency selective multipath fading environment modeled by the aeronautical telemetry channel. In the presence of a strong specular multipath reflection, the ARTM Tier-1 waveforms experience a loss in performance well approximated by (3.27). Analysis of the average bit error probability shows that a relatively high error floor at approximately 10^{-2} occurs for $|\Gamma_1| \geq 0.5$. Thus, the ARTM Tier-1 waveforms possess twice the spectral efficiency of PCM/FM, but exhibit a greater loss and higher error floors than PCM/FM for the same multipath conditions and signal-to-noise ratio.

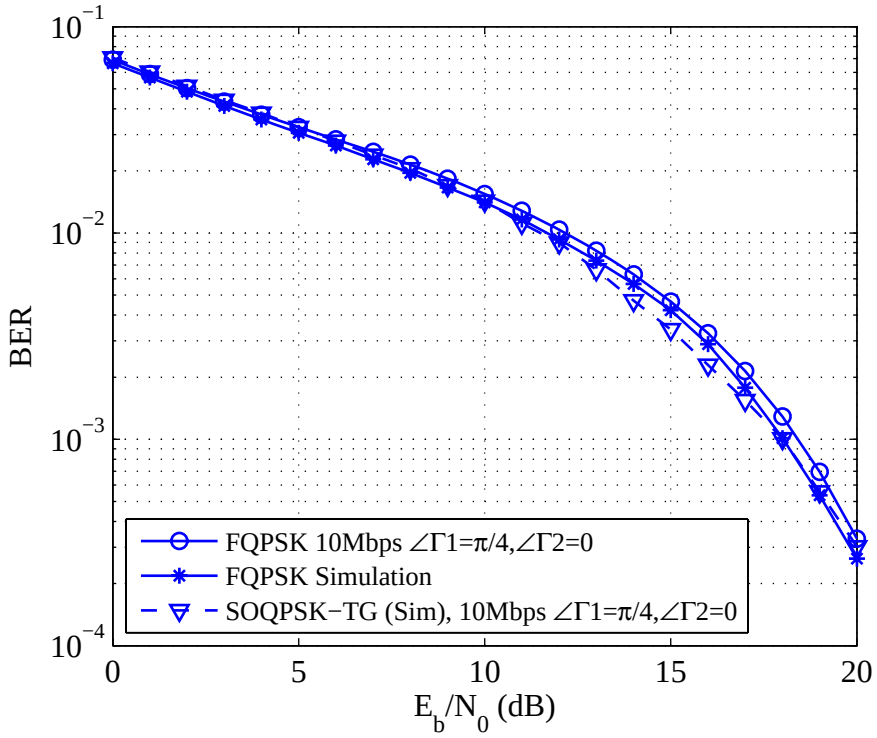

Figure 3.6: Probability of bit error versus E_b/N_0 for 10 Mbit/sec SOQPSK in a multipath fading channel with $\Gamma_1 = 0.85e^{j\pi/4}$, $\tau_1 = 45$ nsec, $\Gamma_2 = 0.01$, $\tau_2 = 155$ nsec. The performance of FQPSK in the same multipath environment is shown for comparison.

Chapter 4

Space-time Trellis Coded Offset QPSK in MIMO Environment

For wireless links with significant power and bandwidth constraints, CPM and offset QPSK (OQPSK) are preferred for use with RF power amplifiers operating in full saturation. When the use of multiple transmit and/or receive antennas is possible, the benefits of mulitple-input, multiple-output (MIMO) communications is desirable. Space-time codes, in the form of space-time trellis codes [2] or space-time block codes [10, 11], is a popular way to realize many of the benefits MIMO has to offer.

With CPM, a space-time code cannot be applied directly to the symbols because there is no way to preserve the continuous phase property and the associated memory in the data symbol sequence [18, 19]. Application of space-time trellis codes for CPM has been investigated by Zhang and Fitz [18], Aygolu and Celebi [20], Cavers [1], Cheng and Lu [43], Yang, Chern, Shiu, and Lee [44], and Altunbas [45], to name a few. Much of the work has focused on MSK and GMSK. Of this work, Cavers' approach [1] is the most closely related to offset QPSK. Cavers used the differentially encoded OQPSK interpretation of MSK[1] to develop a technique that can be generally applied to offset QPSK. The analysis showed that ML detection must function in the presence of correlated noise and that I/Q interference is an unavoidable factor reducing the bit error rate performance. Space-time block coding for CPM has been explored by Yao and Howlader [47] and Silvester et al [3]. The approach described by Silvester is interesting in that space-time block codes were applied to CPM using what they termed "burst based" coding. Instead of applying an orthogo-

[1]The differentially encoded OQPSK interpretation of MSK is a special case of Laurent's PAM representation [46] and could be considered in the context of similar approaches to CPM with space-time coding [18, 44]. But in this chapter, it is more productive to view it explicitly as an approach for OQPSK.

nal space-time block code to symbols, the orthogonal space-time block code is applied to the waveforms that constitute an entire burst. This approach preserves the desirable properties of the modulation and permits the use of single-input, single-output detection techniques.

Space-time block codes with OQPSK have been investigated by Nelson, Rice and others [48, 49, 50, 51]. This work showed that the simple detectors characteristic of non-offset QPSK do not carry over to the OQPSK case. A sequence detector, capable of operating with correlated noise samples, is required even when very simple space-time block codes are used. To my knowledge, the only work involving space-time trellis codes and offset QPSK was Cavers' work on MSK introduced above.

In this chapter, the use of Silvester's burst based block coding [3] is coupled with space-time trellis coded OQPSK. This technique produces an equivalent system that is similar to the system generated by Cavers' approach to MSK [1], but with some key differences. It is shown that the benefits of this approach are the elimination of the correlated noise samples at the input to the space-time decoder and the elimination of the I/Q interference characteristic of the previously published approaches. The benefits (better bit error rate performance and reduced complexity sequence detectors) are achieved at the expense of data rate.

4.1 System Model

In general, a multiple-input, multiple-output (MIMO) wireless communication system consists of M_T transmit antennas and M_R receive antennas. To simplify notation, an $M_T = 2$, $M_R = 1$ system is used to introduce the basic ideas of this chapter in Section 4.1.1. The generalizations are outlined in Section 4.1.2.

4.1.1 A Simple System

The simple $M_T = 2$, $M_R = 1$ system is illustrated in Figure 4.1, which shows the transmitter, the receiver, and the equivalent channel seen by the space-time encoder/decoder pair. These systems are described in the following.

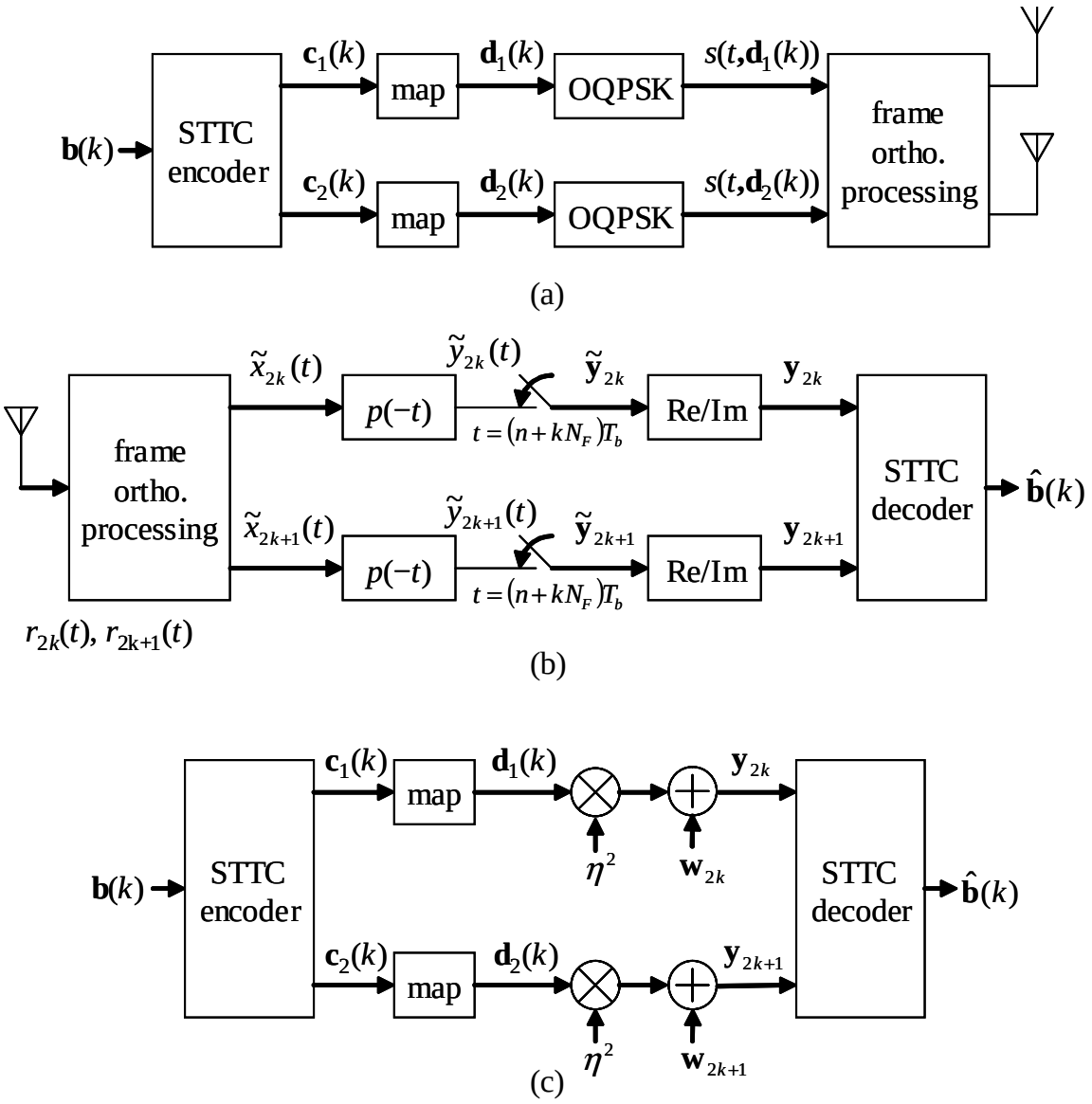

Figure 4.1: An example of an $M_T = 2$, $M_R = 1$ system using space-time trellis codes and waveform orthogonalization: (a) the transmitter; (b) the receiver; (c) the equivalent system seen by the space-time trellis code.

Transmitter

The transmitter is shown in Figure 4.1 (a). Assume the data to be transmitted are organized into frames consisting of N_F bits and let $k = 0, 1, 2, \cdots$ be the frame index. Let $\mathbf{b}(k) = [b(kN_F+1), b(kN_F+2), \ldots, b(kN_F+N_F)]$ be the N_F bits corresponding to the k-th frame. This frame is the input to a space-time trellis encoder that pro-

duces $M_T = 2$ coded bit frames $\mathbf{c}_0(k) = [c_1(kN_F+1), c_1(kN_F+2), \ldots, c_1(kN_F+N_F)]$ and $\mathbf{c}_1(k) = [c_2(kN_F+1), c_2(kN_F+2), \ldots, c_2(kN_F+N_F)]$. Each space-time coded bit $c_i(kN_F+n) \in \{0,1\}$ is mapped to a space-time coded symbol $d_i(kN_F+n) \in \{-1,1\}$ using $d_i(kN_F+n) = 1-2c_i(kN_F+n)$ for $n = 1, \cdots N_F$ and $i = 1, 2$. Each coded symbol frame $\mathbf{d}_i(k)$ forms the input to an OQPSK modulator. During the time interval $kN_FT_b \leq t < (k+1)N_FT_b$, the modulated signal, $s(t, \mathbf{d}_i(k))$, can be written as

$$s(t,\mathbf{d}_i(k)) = \sqrt{\frac{E_b}{M_T}} \left(\sum_{l=1}^{N_F/2} d_i(kN_F+2l-1)p(t-kN_FT_b-(2l-1)T_b) + j\sum_{l=1}^{N_F/2} d_i(kN_F+2l)p(t-kN_FT_b-2lT_b) \right) \quad (4.1)$$

where E_b is the bit energy, T_b is the coded bit time interval, and $p(t)$ is a unit-energy pulse shape which is assumed to be full response.

The waveform orthogonal processor applies a unitary space-time block code to the *waveform* corresponding to *each frame*. As explained in the introduction, this is done to reduce the complexity of the detector and to improve its performance. How these benefits are achieved is described in the next section. As an illustration, the Alamouti space-time block code can be used for $M_T = 2$. During $2kN_FT_b \leq t < (2k+1)N_FT_b$ time interval, $s(t, \mathbf{d}_1(k))$ and $s(t, \mathbf{d}_2(k))$ are transmitted over antenna 1 and antenna 2, respectively. During the following frame interval, $(2k+1)N_FT_b \leq t < (2k+2)N_FT_b$, $-s^*(t-N_FT_b, \mathbf{d}_2(k))$ and $s^*(t-N_FT_b, \mathbf{d}_1(k))$ are transmitted over antenna 1 and antenna 2, respectively. Note that a data rate reduction by 2 occurs here.[2] In general, the data rate reduction is a function of the rate of the orthogonal space-time block code used.

[2]While the Alamouti space-time block code is a rate-1 code, it behaves as a rate 1/2 code in this application. This is because no expansion in the spatial dimension occurs.

Detector

The maximum likelihood detector is illustrated in Figure 4.1 (b). The received waveform $r_{2k}(t)$ during the interval $2kN_FT_b \leq t < (2k+1)N_FT_b$, may be expressed as

$$r_{2k}(t) = h_1 s(t, \mathbf{d}_1(k)) + h_2 s(t, \mathbf{d}_2(k)) + n_{2k}(t) \tag{4.2}$$

where h_1 and h_2 are the complex-valued channel gains between the receive antenna and transmit antennas 1 and 2, respectively, and $n_{2k}(t)$ is the thermal noise which is modeled as a complex-valued white Gaussian random process with zero mean and power spectral density N_0 W/Hz. The channel gains h_1 and h_2 are zero-mean, unit-variance complex-valued Gaussian random variables. We assume quasi-static operation: the channel gains remain constant over an interval of $M_TN_FT_b$ seconds. (Note that as M_T increases, the duration of the quasi-static assumption must also increase.) During the subsequent time interval, $(2k+1)N_FT_b \leq t < (2k+2)N_FT_b$, the received signal $r_{2k+1}(t)$ is

$$r_{2k+1}(t) = -h_1 s^*(t - N_FT_b, \mathbf{d}_2(k)) + h_2 s^*(t - N_FT_b, \mathbf{d}_1(k)) + n_{2k+1}(t) \tag{4.3}$$

where $n_{2k+1}(t)$ is a different realization of the same random process that produced $n_{2k}(t)$.

Waveform orthogonalization is performed using the "decoding" manipulations corresponding to the space-time block code used by the transmitter. For the Alamouti space-time block code, the waveforms $r_{2k}(t)$ and $r_{2k+1}(t)$ are arranged into a waveform vector $\mathbf{R}(t)$

$$\mathbf{R}(t) = \begin{bmatrix} r_{2k}(t) \\ r^*_{2k+1}(t) \end{bmatrix} \tag{4.4}$$

which may be expressed as

$$\mathbf{R}(t) = \begin{bmatrix} h_1 & h_2 \\ h_2^* & -h_1^* \end{bmatrix} \begin{bmatrix} s(t, \mathbf{d}_1(k)) \\ s(t, \mathbf{d}_2(k)) \end{bmatrix} + \begin{bmatrix} n_{2k}(t) \\ n^*_{2k+1}(t) \end{bmatrix} \tag{4.5}$$

where, the time delay by $N_F T_b$ has been removed in the waveforms received during the interval $(2k+1)N_F T_b \leq t < (2k+2)N_F T_b$. The stacking creates an equivalent 2×2 MIMO channel with $s(t, \mathbf{d}_1(k))$ and $s(t, \mathbf{d}_2(k))$ as the inputs and

$$\mathbf{H}_e = \begin{bmatrix} h_1 & h_2 \\ h_2^* & -h_1^* \end{bmatrix} \tag{4.6}$$

as the 2×2 MIMO channel. Because $\mathbf{H}_e^H \mathbf{H}_e = \eta^2 \mathbf{I}$ for $\eta^2 = |h_1|^2 + |h_2|^2$, the equivalent MIMO system may be orthogonalized by multiplying both sides of (4.5) by $\mathbf{H}_e^H$. The result is

$$\tilde{\mathbf{X}}(t) = \begin{bmatrix} \tilde{x}_{2k}(t) \\ \tilde{x}_{2k+1}(t) \end{bmatrix} = \eta^2 \begin{bmatrix} s(t, \mathbf{d}_1(k)) \\ s(t, \mathbf{d}_2(k)) \end{bmatrix} + \begin{bmatrix} \tilde{n}_{2k}(t) \\ \tilde{n}_{2k+1}^*(t) \end{bmatrix} \tag{4.7}$$

where

$$\begin{bmatrix} \tilde{n}_{2k}(t) \\ \tilde{n}_{2k+1}^*(t) \end{bmatrix} = \mathbf{H}_e^H \begin{bmatrix} n_{2k}(t) \\ n_{2k+1}^*(t) \end{bmatrix} \tag{4.8}$$

consists of two uncorrelated, complex-valued white Gaussian random processes with zero-mean and power spectral densities $\eta^2 N_0$ W/Hz. This produces a model for $\mathbf{X}(t)$ that consists of a real-valued constant scaling the transmitted waveforms plus additive *white* noise. The waveform orthogonalization process decouples the transmitted waveforms. This has the effect of removing the I/Q interference due to the offset in the modulated waveform.

The output of the waveform orthogonalization procedure is processed by a filter matched to the pulse shape of $p(t)$. The matched filter output $\tilde{y}_{2k}(t)$ corresponding to the input $\tilde{x}_{2k}(t)$ is

$$\tilde{y}_{2k}(t) = \eta^2 s(t, \mathbf{d}_1(k)) * p(-t) + \tilde{n}_{2k}(t) * p(-t). \tag{4.9}$$

The matched filter output is sampled at $t = (n + kN_F)T_b$ for $n = 1, 2, \ldots, N_F$ to produce the sequence $\tilde{y}_{2k}(nT_b)$. These samples are stacked to form the $N_F \times 1$ vector

$\tilde{\mathbf{y}}_{2k}$. This vector may be expressed as

$$\tilde{\mathbf{y}}_{2k} = \eta^2 \sqrt{\frac{E_b}{M_T}} \mathbf{P}\mathbf{D}\mathbf{d}_1(k) + \tilde{\mathbf{w}}_{2k} \tag{4.10}$$

where $\mathbf{P}$ is an $N_F \times N_F$ matrix consisting of T_b-spaced samples of the pulse shape autocorrelation function

$$r_p(\tau) = \int_{-\infty}^{\infty} p(t)p(t-\tau)dt. \tag{4.11}$$

Because the unit-energy pulse shape is assumed full response *in the symbol time*, $r_p(nT_b)$ is

$$r_p(nT_b) = \begin{cases} \alpha & n = \pm 1 \\ 1 & n = 0 \\ 0 & \text{otherwise} \end{cases} . \tag{4.12}$$

As a consequence, $\mathbf{P}$ is a tri-diagonal matrix of the form

$$\mathbf{P} = \begin{bmatrix} 1 & \alpha & & & \\ \alpha & 1 & \alpha & & \\ & \alpha & 1 & \alpha & \\ & & & \ddots & \\ & & & \alpha & 1 \end{bmatrix} \tag{4.13}$$

where the zeros have been omitted for clarity. The matrix $\mathbf{D}$ is an $N_F \times N_F$ diagonal matrix that separates the inphase and quadrature components of OQPSK and is given by

$$\mathbf{D} = \begin{bmatrix} 1 & & & & \\ & j & & & \\ & & 1 & & \\ & & & \ddots & \\ & & & & j \end{bmatrix} \tag{4.14}$$

(where again the zeros have been omitted for clarity). The vector $\tilde{\mathbf{w}}_{2k}$ is an $N_F \times 1$ vector whose n-th component is $\tilde{w}_{2k}((n + kN_F)T_b)$ (for $n = 1, 2, \ldots, N_F$) where $\tilde{w}_{2k}(t) = \tilde{n}_{2k}(t) * p(-t)$. The elements of $\mathbf{w}_{2k}$ are jointly Gaussian zero-mean complex-valued Gaussian random variables with autocorrelation matrix

$$\mathbf{C} = \eta^2 N_0 \mathbf{P}. \tag{4.15}$$

Similarly, the vector of sampled matched filter outputs due to the input $\tilde{x}_{2k+1}(t)$ is

$$\tilde{\mathbf{y}}_{2k+1} = \eta^2 \sqrt{\frac{E_b}{M_T}} \mathbf{P}\mathbf{D}\mathbf{d}_2(k) + \tilde{\mathbf{w}}_{2k+1} \tag{4.16}$$

where $\tilde{\mathbf{w}}_{2k+1}$ is obtained from $\tilde{n}^*_{2k+1}(t)$ in the same way $\tilde{\mathbf{w}}_{2k}$ is from $\tilde{n}_{2k}(t)$.

Two observations are important:

1. The desired signal in (4.10) and (4.16) is readily available from the real parts of odd-indexed components and the imaginary parts of the even-indexed components.

2. While the noise samples in the vectors $\mathbf{w}_{2k}$ and $\mathbf{w}_{2k+1}$ are correlated, the samples from every other element are uncorrelated. (This follows from the tri-diagonal structure of $\mathbf{P}$.) Because the real and imaginary components of each random variable are also uncorrelated, retaining the real parts of the odd-indexed components and the imaginary parts of the even-indexed components produces a sequence of i.i.d. *real*-valued Gaussian random variables.

Motivated by these observations, the vector $\mathbf{y}_{2k}$ is formed from $\tilde{\mathbf{y}}_{2k}$ as follows:

$$y_{2k}(n) = \begin{cases} \mathrm{Re}\left\{\tilde{y}_{2k}(n)\right\} & n \text{ odd} \\ \mathrm{Im}\left\{\tilde{y}_{2k}(n)\right\} & n \text{ even} \end{cases} \tag{4.17}$$

for $n = 1, 2, \ldots, N_F$. The vector $\mathbf{y}_{2k}$ may be expressed as

$$\mathbf{y}_{2k} = \eta^2 \sqrt{\frac{E_b}{M_T}} \mathbf{d}_1(k) + \mathbf{w}_{2k} \tag{4.18}$$

where $\mathbf{w}_{2k}$ is sequence of real-valued zero-mean uncorrelated Gaussian random variables with common variance $\eta^2 N_0/2$. In a similar way, $\mathbf{y}_{2k+1}$ is formed from $\tilde{\mathbf{y}}_{2k+1}$ and may be expressed as

$$\mathbf{y}_{2k+1} = \eta^2 \sqrt{\frac{E_b}{M_T}} \mathbf{d}_2(k) + \mathbf{w}_{2k+1} \tag{4.19}$$

where $\mathbf{w}_{2k+1}$ is sequence of real-valued zero-mean uncorrelated Gaussian random variables with common variance $\eta^2 N_0/2$. Note that $\mathbf{w}_{2k}$ and $\mathbf{w}_{2k+1}$ are also uncorrelated.

The MLSD decoder computes an estimate of $\mathbf{b}(k)$ from $\mathbf{y}_{2k}$ and $\mathbf{y}_{2k+1}$. The simple structure of (4.18) and (4.19) defines the equivalent system illustrated in Figure 4.1 (c).

4.1.2 The General Case

The case for arbitrary M_T and M_R is illustrated in Figure 4.2. The transmitter, illustrated in Figure 4.2 (a), uses a space-time trellis code to produce N_C parallel bit streams from the input. These bit streams are mapped to symbols and modulated by N_C OQPSK modulators operating in parallel. The N_C waveforms (corresponding to the k-th frame) are applied to an orthogonal space-time block code (OSTBC) defined by an $N_S \times M_T$ matrix with N_C non-zero entries [11]. Note that the OSTBC and STTC share the parameter N_C. The rate of the OSTBC is N_C/N_S. But since the input is already consists of N_C parallel waveforms, application of the OSTBC reduces the data rate by $1/N_S$ to give an overall rate N_C/N_S^2. (In the previous section, $N_C = N_S = M_T = 2$ for the Alamouti space-time block code. This is why the transmitted data rate underwent a reduction by $N_C/N_S^2 = 1/2$.)

The detector, illustrated in Figure 4.2 (b) buffers M_T frames and applies the "decoding" operation corresponding to the OSTBC to generate N_C parallel waveform streams. The waveform streams are applied to a matched filter and sampled at T_b-spaced intervals to produce the samples are used by the STTC decoder. Figure 4.2 (c) illustrates the equivalent channel seen by the STTC encoder/decoder pair.

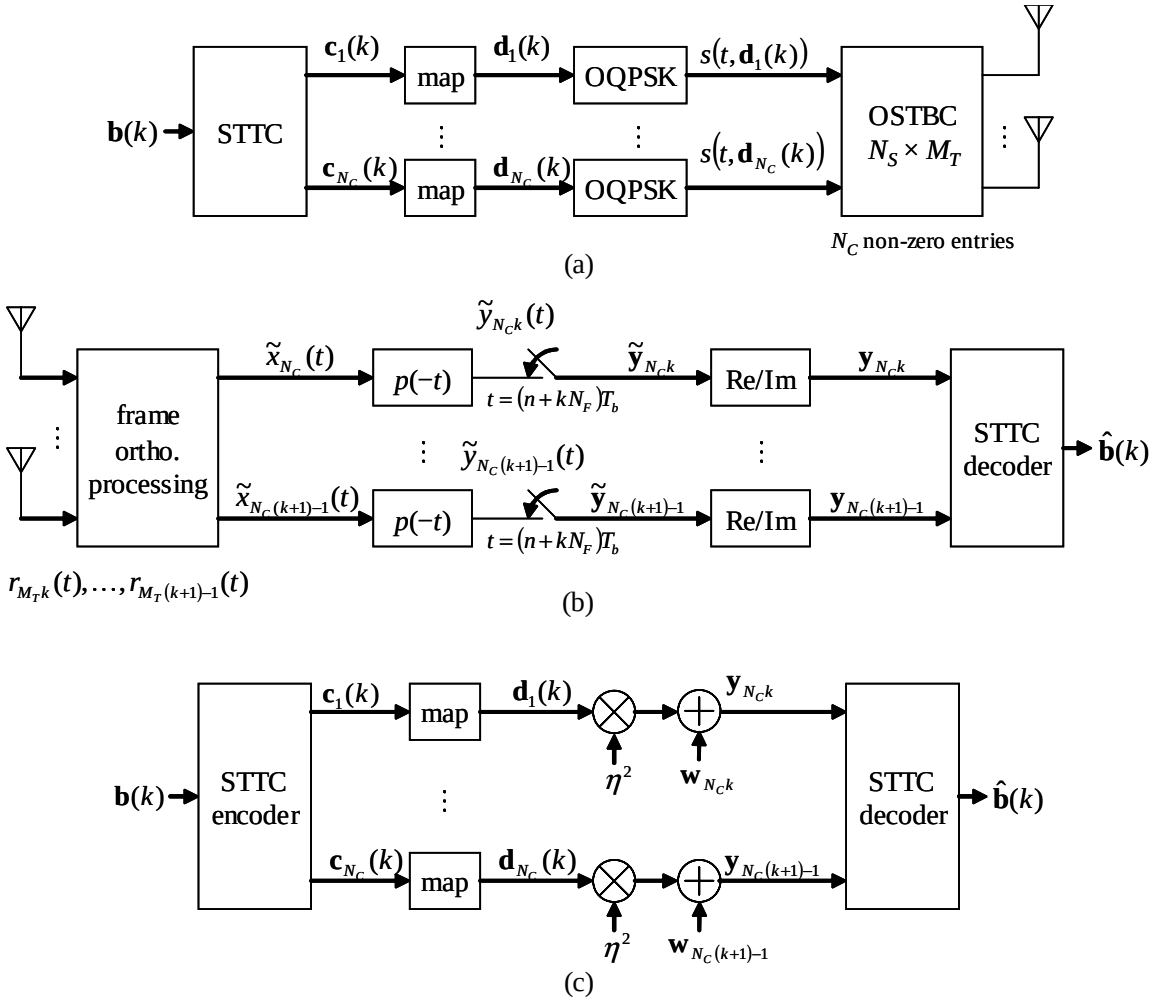

Figure 4.2: The system using space-time trellis codes and waveform orthogonalization using a rate N_C/N_T orthogonal space-time block code: (a) the transmitter; (b) the receiver; (c) the equivalent system seen by the space-time trellis code.

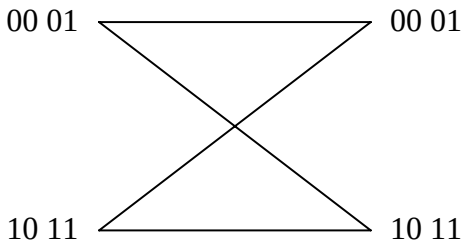

Figure 4.3: The two-state delay diversity space-time trellis code for use with $M_T = 2$ transmit antennas.

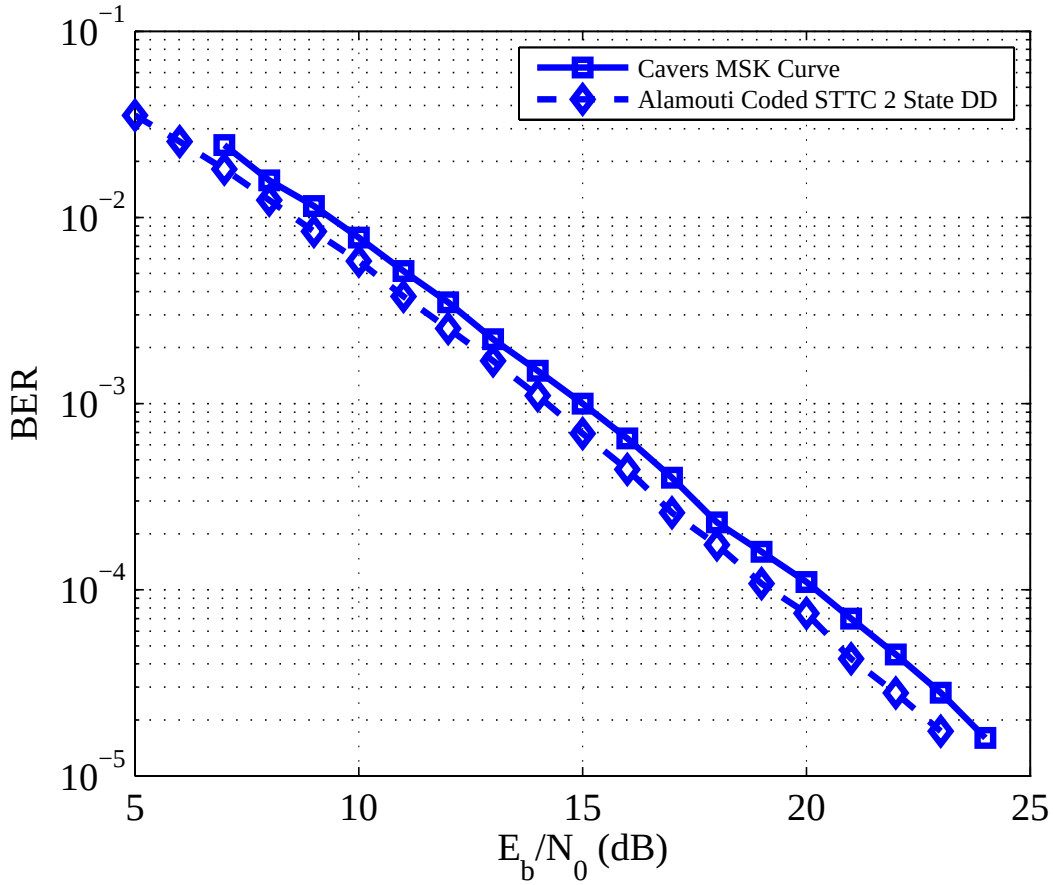

Figure 4.4: Simulated performance of an $M_T = 2$, $M_R = 1$ system for MSK without and with waveform orthogonalization using the Alamouti space-time block code. The squares are from our own simulation of the algorithm described in [1]. The SNR is referenced to the rate-1 signal-to-noise ratio (i.e., the rate-1/2 penalty of the waveform orthogonalization is included).

4.2 Performance Analysis

4.2.1 Union Bound

The Union Bound of a MIMO system of M_T by M_R is derived here. First, we note that from the orthogonal wave-forming, we have the random variable α defined by

$$\alpha = \sum_{i=1}^{M_T M_R} |h_i|^2 = \sum_{i=1}^{M_T M_R} (\mathrm{Re}\{h_i\})^2 + \sum_{i=1}^{M_T M_R} (\mathrm{Im}\{h_i\})^2 \tag{4.20}$$

where $\mathrm{Re}\{h_i\}$ and $\mathrm{Im}\{h_i\}$, $1 \leq i \leq M_T M_R$, are real-valued Gaussian random variables with zero-mean and half-unit variance $\sigma^2 = 1/2$. Since a chi-square random variable is defined by the sum of the squared real Gaussian random variables, we know that α is a chi-square distributed random variable, with $n = 2M_T M_R$ degrees of freedom.

Then the probability density function of α can be denoted by

$$f(\alpha) = \frac{\alpha^{n/2-1}}{2^{n/2}\sigma^n \Gamma(n/2)} \exp\left(-\frac{\alpha}{2\sigma^2}\right) \tag{4.21}$$

where $\Gamma(n/2) = (n/2-1)!$.

The advantage of the orthogonal wave-forming changes the complex Gaussian channels h_i's into a single chi-squared random variable α, which leads to the signal-noise ratio at the receiver

$$\mathrm{SNR} = \frac{2\alpha E_b}{M_T N_0}. \tag{4.22}$$

According to Ref [36], the performance bound for a SISO convolution code can be expressed in the following form

$$P_e \leq \sum_{d=d_{\mathrm{free}}}^{\infty} K(d) Q\left(\sqrt{\frac{2R_c E_b d}{N_0}}\right) \tag{4.23}$$

where $K(d)$, the coefficients of the polynomial in transfer function of convolution code, mean the number of paths of distance d from the all-zero path that merge with the all-zero path the first time, d_{free} is the minimum free distance for the convolution code, E_b/N_0 is the received SNR per bit, and R_c is the *temporal* code rate.

Once we have the SISO convolution code performance available, we can smoothly extend this result to a Space-Time trellis code after orthogonal wave-forming. There are two reasons why we can do this: first the trellis structures (generating polynomial, nodes, branches) are all the same; second, the noise after the orthogonal wave-forming is still white both in time and in space. They only change is the chi-squared random variable α which actually generates Rayleigh channels for MISO channels.

So the performance bound for a Space-Time trellis code can be given by

$$P_e \leq \sum_{d=d_{\text{free}}}^{\infty} K(d) Q\left(\sqrt{\frac{2R_c d\alpha E_b}{M_T N_0}}\right) \tag{4.24}$$

which is conditioned on α. Note that $Rc = N_C/N_S^2$ is *the overall space-time* code rate.

We can obtain the exact space-time trellis error performance expression by averaging equation (4.24) over α. Let

$$\beta = \frac{R_c d\alpha E_b}{M_T N_0}, \tag{4.25}$$

then β is a chi-square random variable with parameter

$$\sigma_\beta^2 = \frac{R_c d E_b}{M_T N_0}\sigma^2. \tag{4.26}$$

Now we calculate $E\left(Q\left(\sqrt{2\beta}\right)\right)$, which is the individual expectation of each $Q\left(\frac{2R_c d\alpha E_b}{M_T N_0}\right)$ as in equation (4.24). So we have

$$E\left(Q\left(\sqrt{2\beta}\right)\right) = \int_0^\infty Q\left(\sqrt{2\beta}\right) \frac{\beta^{n/2-1}}{\Gamma(n/2)(2\sigma_\beta^2)^{n/2}} \exp\left(\frac{-\beta}{2\sigma_\beta^2}\right) d\beta. \tag{4.27}$$

There is a closed-form solution for the integral above [36]. When SNR is large, we have

$$E\left(Q\left(\sqrt{2\beta}\right)\right) \approx \left(\frac{1}{8\sigma_\beta^2}\right)^{n/2} \binom{n-1}{n/2}. \tag{4.28}$$

Substituting (4.26) for σ_β produces

$$E\left(Q\left(\sqrt{2\beta}\right)\right) \approx \binom{n-1}{n/2} \left(\frac{4R_c d}{M_T}\frac{E_b}{N_0}\right)^{-M_T M_R}. \tag{4.29}$$

So the final average bit error probability bound is

$$\bar{P}_e \approx \binom{n-1}{n/2} \sum_{d=d_{\text{free}}}^{\infty} K(d) \left(\frac{4R_c d}{M_T}\frac{E_b}{N_0}\right)^{-M_T M_R}. \tag{4.30}$$

We can see that the diversity order of $M_T M_R$ is obtained. For a 2 by 1 MISO system, equation (4.30) reduces to

$$\bar{P}_e = 0.75 \sum_{d=d_{free}}^{\infty} K(d) \left(R_c d \frac{E_b}{N_0} \right)^{-2}. \tag{4.31}$$

The equation (4.30) above shows the diversity order of $M_T M_R$ is achieved in the MIMO system. It also implies that after the wave orthogonalization, different sets of values of $K(D)$ can be generated by a different trellis, so the delay diversity scheme may not be the best trellis code for in terms of the bit error rate performance.

4.2.2 Optimum Space-Time Codes with Waveform Orthogonalization

It is interesting to find the optimum space-time trellis codes under the condition of waveform orthogonalization. It can be seen that after the wave orthogonalization, the MISO or MIMO channels will actually be identical Rayleigh fading channels solely described by real coefficient α, hence the inherent I/Q interference in MISO or MIMO can be completely removed by separating the real and imaginary parts of the received signal. So in the sense of the waveform orthogonalization, the optimum SISO trellis code in the Rayleigh fading will have the optimum BER performance in MISO or MIMO environment.

Table 4.1 shows the basic description of two two-state space-time trellis codes. Because of the nonzero terms of $K(d)$, which directly result in a lower union bound, the trellis code with the generating polynomial $1 + D$ has the optimum bit error rate performance. Similarly, for 4-state or even higher state space-time codes, the available optimum SISO trellis code results in Rayleigh channels, previously investigated by [52], which will still be extended to MISO or MIMO environments if waveform orthogonalization is applied.

4.3 MSK Example

In this section, the waveform orthogonalization technique described in Section 4.1.1 for $M_T = 2$ and $M_R = 1$ is applied to MSK. This is done to facilitate a

direct comparison with previously published results by Cavers [1]. It is well-known that MSK has an equivalent representation as a differentially encoded offset QPSK signal using the half-sine pulse shape. As a consequence, the analysis of Section 4.1.1 applies with a few modifications to account for the differential encoding. The two vectors of sampled matched-filter outputs are modified versions of (4.10) and (4.16) and are given by

$$\tilde{\mathbf{y}}_{2k} = \alpha\sqrt{\frac{E_b}{M_T}}\mathbf{P}\mathbf{D}'\mathbf{d}'_1(k) + \tilde{\mathbf{w}}_{2k}, \tag{4.32}$$

and

$$\tilde{\mathbf{y}}_{2k+1} = \alpha\sqrt{\frac{E_b}{M_T}}\mathbf{P}\mathbf{D}'\mathbf{d}'_2(k) + \tilde{\mathbf{w}}_{2k+1} \tag{4.33}$$

where $\mathbf{D}'$ is a diagonal matrix whose i-th diagonal element $D'(i,i) = (j)^{i-1}$ for $i = 1, 2, \ldots, N_F$ and $\mathbf{d}'_1(k)$ is the vector of differentially encoded symbols where

$$d'_1(kN_F + i) = d_1(kN_F + i)d'_1(kN_f + i - 1) \tag{4.34}$$

for $i = 1, 2, \ldots, N_F$. Note that desired signal is still available from the real parts of the odd-indexed components and the imaginary parts of the even-indexed components.

The well-known "delay diversity" space-time trellis code defined by the two-state trellis in Figure 4.3 is used. (This is the STTC used by Cavers in [1] in a system that can be represented by the block diagrams of Figure 4.1 (a) and (b) except without the OSTBC at the transmitter and receiver.) Direct comparison with the two systems illustrates the potential performance gains of applying the OSTBC for waveform orthogonalization. The following are the main points of the comparison

1. For the system without waveform orthogonalization, the STTC decoder must operate on a trellis in the presence of correlated noise. Cavers addressed this issue in [1] by applying Ungerboeck's technique for sequence estimation. For the system with waveform orthogonalization, the noise samples at the input to the STTC decoder are uncorrelated thereby allowing the less-complex Viterbi algorithm to be used.

2. The performance of the system without waveform orthogonalization suffers from I/Q interference resulting from the presence of two OQPSK waveforms with different phase shifts. Waveform orthogonalization decouples the two signals, thereby removing this I/Q interference.

3. These advantages are achieved at the expense of rate. The system with waveform orthogonalization operates at rate 1/2 the rate of the system without waveform orthogonalization.

The simulated performance of the two systems using $N_F = 260$ bits is shown in Figure 4.4. For both systems, ideal symbol timing synchronization and ideal channel estimation is assumed. Our system, using waveform orthogonalization, included a differential decoder at the transmitter (not shown due to space limitations) to "undo" the differential encoding inherent in the MSK modulation. This was done to remove the differential decoding penalty in bit error rate performance. The simulation results show that the waveform orthogonalization improves the performance approximately 1.2 dB at a bit error rate of 10^{-4}. This improvement is due to the removal of the I/Q interference and the differential decoding penalty.

The performance of this optimum STTC code with the generating polynomial of $1+D$ is shown In Figure 4.5,. With the waveform orthogonalization, this optimum two-state STTC with the generating polynomial of $1+D$ is about 0.6 dB better than the STTC delay diversity scheme. Also the union bound is given to show that the STTC diversity order of M_T is achieved.

4.4 Conclusions

We have shown how orthogonal space-time block codes can be applied *to waveforms* to orthogonalize a space-time coded multiple-input, multiple-output link. For offset QPSK, this technique has the advantage of eliminating the I/Q interference associated with simultaneous transmission of offset QPSK waveforms. In addition, orthogonalization presents uncorrelated noise samples to the space-time trellis decoder. As a consequence, a less complex space-time decoder (relative to what would

Table 4.1: Comparison of two space-time trellis codes

Generator Polynomial	D	$1+D$
d_{free}	2	3
Transfer Function	$\frac{D^2}{1-D^2}$	$\frac{D^3}{1-D}$
$K(d), (d \geq d_{free})$	$1, 0, 1, 0 \cdots$	$1, 1, 1, 1 \cdots$

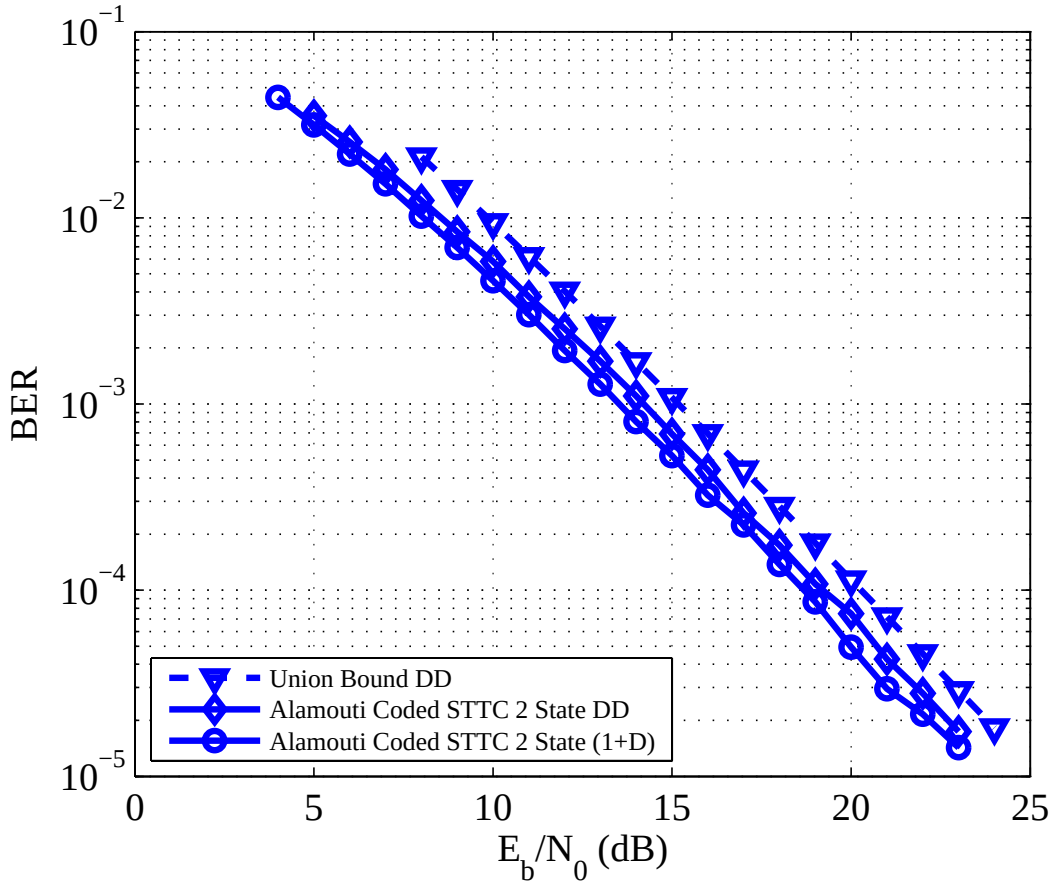

Figure 4.5: Simulated performance of an $M_T = 2$, $M_R = 1$ system for MSK without and with waveform orthogonalization using the Alamouti space-time block code and $1+D$ as the STTC scheme. The SNR is referenced to the rate-1 signal-to-noise ratio (i.e., the rate-1/2 penalty of the waveform orthogonalization is included), as in Figure 4.4.

be required without orthogonalization) can be used. These benefits are achieved at the expense of data rate as described. Also the optimum STTC-trellis code is based on waveform orthogonalization, which is the direct extension of the available optimum of SISO codes to MISO or MIMO environments.

Chapter 5

Space-time Trellis Codes and Concatenated Trellis-Coded Orthogonal Space-time Block Codes: A Performance and Complexity Comparison

Tarokh's seminal paper [2] introduced space-time trellis codes, derived design criteria for the codes, and listed good trellis codes for systems with 2 receive antennas. A conceptual block diagram for a system consisting of N_T transmit antennas and N_R receive anteannas is illustrated in Figure 5.1 (a). The modulations considered in [2] were linear, non-offset modulations (QPSK, 8PSK, and 16-QAM). For this reason, the diagram in Figure 5.1 (a) focuses on the symbols.

The application of space-time trellis codes to offset modulations has proven more challenging. As we mentioned in previous chapter, Silvester's method [3]. involves orthogonal space-time block codes, based on complex orthogonal designs [11], and bursts of CPM waveforms. The essentials of the system are summarized in Figure 5.1 (b). A rate $R_C = N_C/N_S$ complex orthogonal design transmits N_C indeterminants over N_T transmit antennas during N_S time slots. The corresponding orthogonal space-time block code is described by an $N_S \times N_T$ matrix involving N_C indeterminants and their conjugates. Given N_C parallel data streams of finite length, the Silvester system produces N_C CPM bursts. The CPM bursts are processed by the orthogonal space-time block code where each *burst* is treated as the indeterminant in the space-time block code. The resulting N_T parallel CPM waveforms are transmitted from the N_T transmit antennas. At the output of the MIMO channel, the N_R waveforms are combined, following the "decoding" rules corresponding to the space-time block code, to produce N_C noisy waveform bursts that can be treated as the outputs of N_C independent single-input, single-output fading channels. The role

of the orthogonal space-time block code is to orthogonalize the waveform channel on a burst-by-burst basis.

The approach described by Silvester does not have to be applied to N_C CPM waveforms operating in parallel. This approach could be used with a linear modulation in combination with a trellis code designed for a single-input/single-output fading channel. An example is illustrated in Figure 5.2. Using a rate-k/N_C trellis code, N_C parallel coded symbols are produced for each input block of k symbols. The N_C coded symbols are "encoded" by the rate N_C/N_S orthogonal space-time block code to produce a new block of symbols that is transmitted by sending N_T symbols in parallel over N_S symbol times. The receiver combines the N_R outputs of the MIMO channel following the space-time combining defined by the orthogonal space-time block code. After space-time combining, the ML decoder (corresponding to the rate-k/N_C trellis code) produces an estimate of the input bits. We refer to this arrangement using the unfortunately verbose concatenated trellis-coded orthogonal space-time coded (CTO) system.

The motivation for considering such an arrangement is as follows:

1. The orthogonal space-time block code orthogonalizes the system in the sense that the inputs to the ML decoder are N_C parallel decision variables, scaled by a *common* fading constant and perturbed by uncorrelated Gaussian random variables.

2. The orthogonalization maximizes the opportunity for diversity gain.

3. The orthogonalization simplifies trellis and its corresponding computations by eliminating noise and spatial correlation between the parallel decision variables.

4. The orthogonalization allows the use of trellis codes optimized for single-input, single-output fading channels.

These advantages are obtained at the expense of rate. Because the trellis code is used to fill the spatial dimension, the "spatial" dimension of the orthogonal space-time

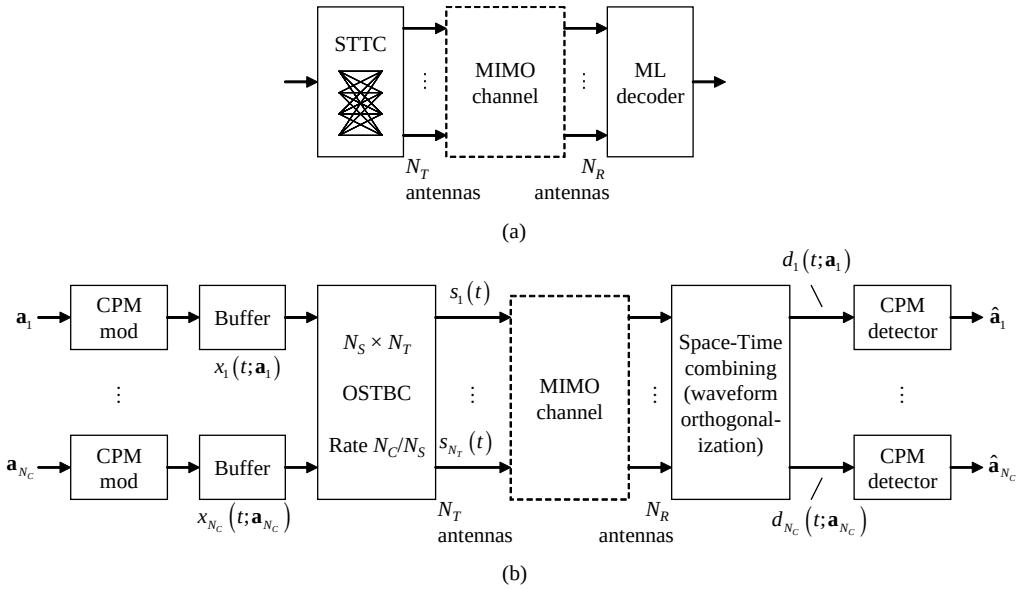

Figure 5.1: The two general types of space-time coded MIMO systems considered in this chapter: (a) The space-time trellis code (STTC) described by Tarokh, et. al. in [2]. The equivalent *symbol*-based representation is shown. (b) The burst-orthogonalization MIMO system described by Silvester, et. al. in [3]. The complex-baseband waveform representation is used because the orthogonal space-time block code (OSTBC) operates on waveforms. Silvester described this system in the context N_C parallel CPM waveforms.

block code is used for temporal expansion to create an orthogonal system between the trellis encoder and the ML decoder.

Given the advantages of orthogonalization and the associated rate penalty, it is an open question as to whether the CTO system outperforms an STTC system. This chapter answers this question. We demonstrate that for a given rate, two transmit antennas, and one receive antenna, the CTO system outperforms the STTC system both in terms of error performance and complexity.

5.1 System Model

Consider a communication system with $N_T = 2$ transmit antennas and $N_R = 1$ receive antenna. At symbol time k, symbols $a_1(k)$ and $a_2(k)$, drawn from a finite alphabet defined by an M-ary constellation, are transmitted from antennas 1 and 2, respectively. Transmission is accomplished by applying unit-energy pulse shaping in

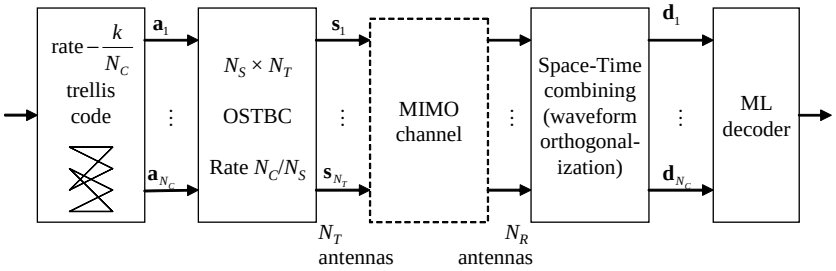

Figure 5.2: A block diagram of the application of Silvester's burst orthogonalization MIMO system to a trellis-coded system using a linear modulation.

the usual manner to produce the complex-valued baseband equivalent signals $s_1(t)$ and $s_2(t)$, respectively. These signals propagate over a frequency non-selective fading channel characterized by h_1 and h_2, the complex-valued random attenuations between transmit antennas 1 and 2 and the receive antenna, respectively. The received signal is

$$r(t) = h_1 s_1(t) + h_2 s_2(t) + w(t) \tag{5.1}$$

where $w(t)$ is the additive thermal noise modeled as a zero-mean complex-valued Gaussian random process whose real and imaginary parts each have a power spectral density $N_0/2$ W/Hz. The channel fading gains h_1, h_2, are modeled as uncorrelated complex-valued Gaussian random variables each with zero mean. The variance of the real and imaginary parts of each fading gain is $1/2$.

The received signal is processed by a filter matched to the pulse shape. Assuming ideal frequency and symbol timing synchronization, the matched filter output is

$$r(k) = h_1 a_1(k) + h_2 a_2(k) + w(k) \tag{5.2}$$

where $w(k)$ is a complex-valued Gaussian random variable with zero mean whose real and imaginary parts have variance $N_0/2$.

5.1.1 Space-Time Trellis Codes

A block diagram of an $N_T = 2$, $N_R = 1$ system based on the use of space-time trellis codes is illustrated in Figure 5.3. The spectral efficiency is determined by the

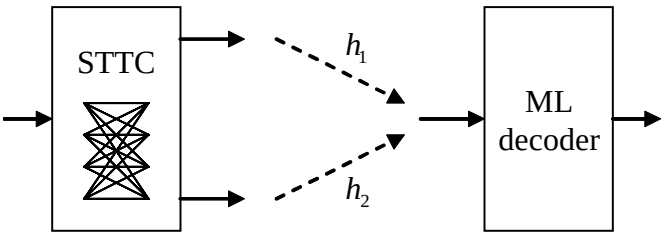

Figure 5.3: Tarokh's space-time trellis coded system with $N_T = 2$ and $N_R = 1$.

size of the constellation and the amount of temporal expansion. The average error probability is computed by averaging the pairwise error probabilities in the usual manner. The pairwise error probability for the system is [2]

$$P_2(E) = \left(\prod_{i=1}^{r} \lambda_i \right)^{-1} \left(\frac{E_b}{2N_0} \right)^{-r} \tag{5.3}$$

where λ_1 and λ_2 are the singular values of the pairwise error matrix $\mathbf{A}(\mathbf{c}, \mathbf{e})$ and $r \leq 2$ is the number of non-zero eigenvalues of $\mathbf{A}(\mathbf{c}, \mathbf{e})$. A pairwise error event occurs when two paths through the code trellis diverge and remerge after L time steps. The pairwise error matrix corresponding to this event is

$$\mathbf{A}(\mathbf{c}, \mathbf{e}) = \begin{bmatrix} \sum_{t=0}^{L} (c_t^1 - e_t^1)(c_t^1 - e_t^1)^* & \sum_{t=0}^{L} (c_t^1 - e_t^1)(c_t^2 - e_t^2)^* \\ \sum_{t=0}^{L} (c_t^2 - e_t^2)(c_t^1 - e_t^1)^* & \sum_{t=0}^{L} (c_t^2 - e_t^2)(c_t^2 - e_t^2)^* \end{bmatrix} \tag{5.4}$$

where

$$\mathbf{c} = \begin{bmatrix} c_0^1 & c_1^1 & \cdots & c_L^1 \\ c_0^2 & c_1^2 & \cdots & c_L^2 \end{bmatrix} \tag{5.5}$$

is a code matrix (or "codeword") where the element c_t^n is the symbol (or constellation point) transmitted from antenna n during time step t. The code matrix $\mathbf{e}$ is defined similarly.

5.1.2 CTO Systems

A block diagram of an $N_T = 2$, $N_R = 1$ CTO system based on the Alamouti space-time block code [10] ($N_C = 2$, $N_S = 2$) is illustrated in Figure 5.4 (a). The equivalent system, as seen by the trellis encoder and decoder pair, is illustrated in Figure 5.4 (b). Note that that the use of the orthogonal space-time block code at the transmitter and the "decoder" or space-time combiner at the receiver orthogonalizes the channel as described by [3]. The trellis code produces $N_C = 2$ parallel length-N symbol streams organized into the vectors $\mathbf{a}_1$ and $\mathbf{a}_2$. After space-time combining, the $N_C = 2$ inputs to the ML decoder are the vectors $\mathbf{r}_1$ and $\mathbf{r}_2$, given by

$$\mathbf{r}_1 = \alpha\mathbf{a}_1 + \mathbf{w}_1 \qquad \text{and} \qquad \mathbf{r}_2 = \alpha\mathbf{a}_2 + \mathbf{w}_2 \tag{5.6}$$

where $\alpha = |h_1|^2 + |h_2|^2$ is a chi-square random variable with 4 degrees of freedom and $\sigma_\alpha^2 = 1$ and $\mathbf{w}_1$ and $\mathbf{w}_2$ are uncorrelated Gaussian random vectors where each vector consists of i.i.d. complex-valued Gaussian random variables with zero mean whose real and imaginary parts have variance $N_0/2$.

For a rate k/N_C trellis code based on symbols from an M-ary constellation and a rate $R_C = N_C/N_S$ orthogonal space-time block code described by an $N_R \times N_S$ matrix, the rate of the CTO system is

$$R_{\text{CTO}} = \frac{k\log_2(M)}{N_S} = \frac{k\log_2(M)}{2} \text{ bits/channel use.} \tag{5.7}$$

The probability of error for the CTO system is quantified using the union bound on pairwise error probabilities. The conditional pairwise error probability between a codeword $\mathbf{c}$ and $\mathbf{e}$ is

$$P_2(E|\alpha) = Q\left(\sqrt{\frac{2\alpha d^2(\mathbf{c},\mathbf{e})R_{\text{CTO}}E_b}{N_0}}\right) \tag{5.8}$$

where

$$d^2(\mathbf{c},\mathbf{e}) = \frac{|\mathbf{c}-\mathbf{e}|^2}{E_b} \tag{5.9}$$

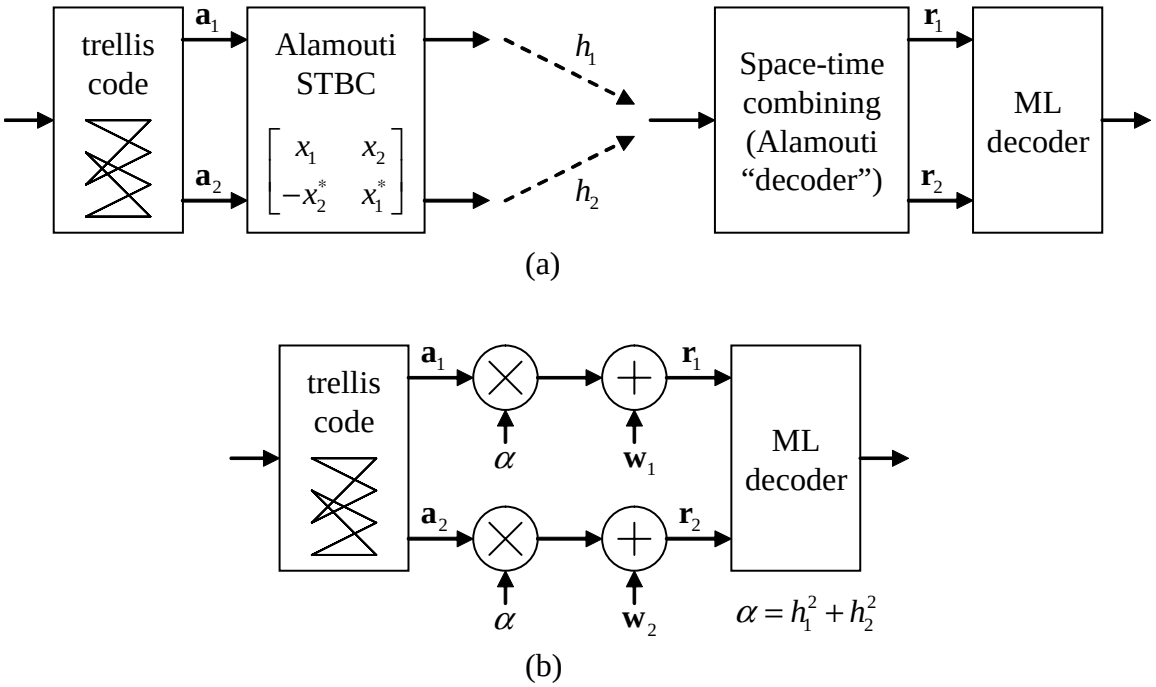

Figure 5.4: A CTO system with $N_R = 2$ and $N_R = 1$ using a rate 1/2 space-time trellis code concatenated with the Alamouti space-time block code. (a) The high level system model showing the trellis code as the inner code and the Alamouti space-time block code as the outer code. (b) The equivalent system seen by the outer code.

is the normalized squared Euclidean distance between the codewords $\mathbf{c}$ and $\mathbf{e}$. The conditional probability $P_2(E|\alpha)$ is of the form $Q(\sqrt{2\beta})$ where $\beta = \alpha d^2(\mathbf{c},\mathbf{e})R_{\text{CTO}}E_b/N_0$ is a chi-square random variable with 4 degrees of freedom and $\sigma_\beta^2 = d^2(\mathbf{c},\mathbf{e})R_{\text{CTO}}E_b/N_0$. The average probability of error is

$$\begin{aligned} P_2(E) &= \int_0^\infty Q\left(\sqrt{2\beta}\right) \frac{\beta}{\Gamma(2)(2\sigma_\beta^2)^2} \exp\left(-\frac{\beta}{2\sigma_\beta^2}\right) d\beta \\ &\approx 3\left(\frac{1}{8\sigma_\beta^2}\right)^2 = \frac{3}{64}\left(\frac{d^2(\mathbf{c},\mathbf{e})R_{\text{CTO}}E_b}{N_0}\right)^{-2} \end{aligned} \tag{5.10}$$

where the approximation is valid for large $E_b/N_0 >> 1$.

5.2 Comparisons

5.2.1 $N_T = 2$, $N_R = 1$ Systems with Rate 1 bit/channel use

The simplest CTO system is one based on a rate-1/2 trellis code with QPSK. This system achieves a rate of

$$R_{\text{CTO}} = \frac{\log_2(4)}{2} = 1 \text{ bit/channel use.} \tag{5.11}$$

In this comparison, we use the simple two-state trellis code described in [31]. The trellis description of this code contains two length-2 paths whose normalized Euclidean distance is 4 with each path producing 2 bit errors; and one path whose normalized Euclidean distance is 8 that produces 4 bit errors. This information is used in (5.10) and averaged to produce the bit error probability curve for the CTO system shown in Figure 5.6.

The QPSK-based STTC that operates at 1 bit/channel use is Tarokh's "smart-greedy" space-time code. Smart-greedy space-time codes incorporate a temporal expansion (with an accompanying reduction in rate) to improve the error rate performance of the code. Consider the smart-greedy code described in Section III.I of [2] based on QPSK: the code matrices are composed of elements

$$e_t^n, e_t^n \in \left\{ e^{j\pi/4}, e^{j3\pi/4}, e^{j5\pi/4}, e^{j7\pi/4} \right\}.$$

The shortest error events for this code remerge at the 3rd time step. Consequently, the pairwise error matrix for these events is of the form (5.4) with $L = 3$. Using

$$\mathbf{c} = \begin{bmatrix} c_0^1 & c_1^1 & c_2^1 & c_3^1 \\ c_0^2 & c_1^2 & c_2^2 & c_3^2 \end{bmatrix} = \begin{bmatrix} e^{j\pi/4} & e^{j\pi/4} & e^{j\pi/4} & e^{j\pi/4} \\ e^{j\pi/4} & e^{j\pi/4} & e^{j\pi/4} & e^{j\pi/4} \end{bmatrix}$$

as the transmitted code matrix, there are three other code matrices of interest. These code matrices, along with the corresponding non-zero eigenvalues of the resulting

pairwise error matrix $\mathbf{A}(\mathbf{c}, \mathbf{e})$ are

$$\mathbf{e} = \begin{bmatrix} e^{j\pi/4} & e^{j\pi/4} & e^{j3\pi/4} & e^{j3\pi/4} \\ e^{j3\pi/4} & e^{j3\pi/4} & e^{j\pi/4} & e^{j\pi/4} \end{bmatrix} \rightarrow \lambda_1 = 4, \lambda_2 = 4,$$

$$\mathbf{e} = \begin{bmatrix} e^{j\pi/4} & e^{j\pi/4} & e^{j3\pi/4} & e^{j5\pi/4} \\ e^{j3\pi/4} & e^{j5\pi/4} & e^{j\pi/4} & e^{j\pi/4} \end{bmatrix} \rightarrow \lambda_1 = 6, \lambda_2 = 6,$$

and

$$\mathbf{e} = \begin{bmatrix} e^{j\pi/4} & e^{j\pi/4} & e^{j3\pi/4} & e^{j7\pi/4} \\ e^{j3\pi/4} & e^{j7\pi/4} & e^{j\pi/4} & e^{j\pi/4} \end{bmatrix} \rightarrow \lambda_1 = 4, \lambda_2 = 4.$$

These values are used in (5.3) to approximate the error rate. The bit error rate is approximated by dividing (5.3) by $\log_2(M) = 2$.

The average probability of bit error for CTO and STTC systems is illustrated in Figure 5.6. This plot shows that the error probability for the CTO system is slightly better than that of the smart-greedy STTC. However, as the expressions used to generate the plots are approximations, the most that can be concluded is that the bit error rate performance of the two is comparable.

For complexity, the number of real-valued multiplications for the two schemes are compared. A generic n_s-state trellis code based on QPSK requires a trellis with n_s nodes at each stage, 4 branches per node, and 2 complex-by-complex multiplications to compute the branch metrics for each branch. The total number of real-valued multiplications is $32n_s$ for each trellis stage. The code used in the CTO system considered here was designed to reduce the required complexity. With this code, the inphase and quadrature components are separable so that the decoder operates 2 n_s-state trellises in parallel. Each node in the trellis has 2 branches and the branch metrics require 2 real-valued multiplications. Including the multiplications required to perform the Alamouti "decoding," the complexity is

$$M_{\text{CTO}} = 8n_s + 8 = 24 \tag{5.12}$$

real valued multiplications per stage (per two-bit symbol). In comparison, an n_s-state smart-greedy STTC requires a decoder with an n_s-state trellis with 4 branches at each node and 4 complex-by-complex multiplications for each branch metric. The computational load is

$$M_{\text{STTC}} = 64n_s = 128 \tag{5.13}$$

real-valued multiplications for each block of 2 output bits. From this we conclude that the 2-state smart-greedy STTC is roughly 5 times more complex than the CTO system based on the 2-state code of [31]. We note that the orthogonalization produced by the Alamouti processing is what makes the complexity reduction possible. The complexity comparison are shown in Figure 5.5.

5.2.2 $N_T = 2$, $N_R = 1$ Systems with Rate 2 bits/channel use

The diversity-optimum STTC based on QPSK achieves 2 bits/channel use. The 8-state QPSK STTC described in Section III.B of [2] is considered here. (The 8-state code is used because the CTO system described below is based on an 8-state trellis code.) For this code, there is one length-2 error event associated with

$$\mathbf{c} = \begin{bmatrix} e^{j\pi/4} & e^{j\pi/4} \\ e^{j\pi/4} & e^{j\pi/4} \end{bmatrix} \quad \mathbf{e} = \begin{bmatrix} e^{j\pi/4} & e^{j5\pi/4} \\ e^{j5\pi/4} & e^{j\pi/4} \end{bmatrix}. \tag{5.14}$$

This error event produces a pairwise error matrix $\mathbf{A}(\mathbf{c}, \mathbf{e})$ with 2 non-zero eigenvalues: $\lambda_1 = 4, \lambda_2 = 4$. There are two length-3 error events associated with

$$\mathbf{c} = \begin{bmatrix} e^{j\pi/4} & e^{j\pi/4} & e^{j\pi/4} \\ e^{j\pi/4} & e^{j\pi/4} & e^{j\pi/4} \end{bmatrix}. \tag{5.15}$$

The pairwise error matrix for these error events is of the form (5.4) with $L = 2$. The error code matrices, along with the corresponding non-zero eigenvalues of the

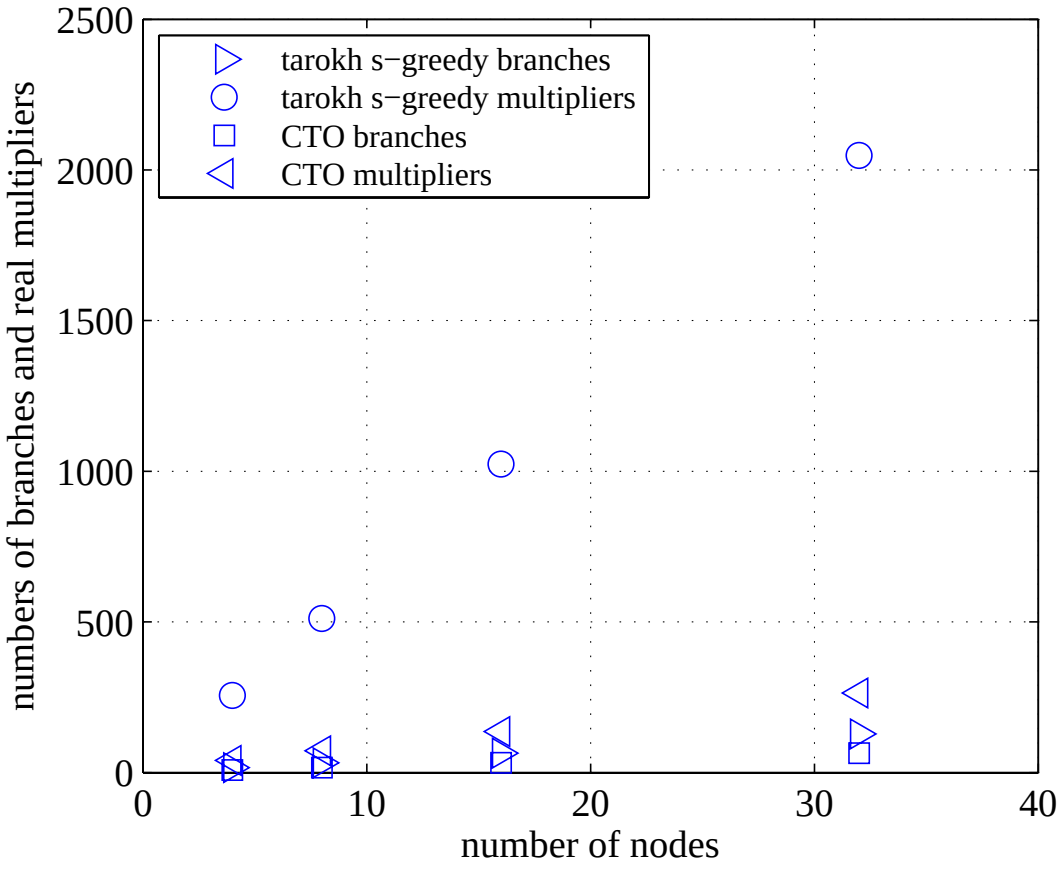

Figure 5.5: The calculation complexity comparison between a QPSK CTO system and a QPSK-based smart-greedy STTC system, both of which achieve a rate of 1 bit/ channel use.

resulting pairwise error matrix $\mathbf{A}(\mathbf{c}, \mathbf{e})$ are

$$\mathbf{e} = \begin{bmatrix} e^{j\pi/4} & e^{j3\pi/4} & e^{j5\pi/4} \\ e^{j3\pi/4} & e^{j\pi/4} & e^{j5\pi/4} \end{bmatrix} \rightarrow \lambda_1 = 2, \lambda_2 = 10,$$

and

$$\mathbf{e} = \begin{bmatrix} e^{j\pi/4} & e^{j7\pi/4} & e^{j5\pi/4} \\ e^{j7\pi/4} & e^{j\pi/4} & e^{j5\pi/4} \end{bmatrix} \rightarrow \lambda_1 = 2, \lambda_2 = 10.$$

Using these values in (5.3) and dividing by $\log_2(M) = 2$ produces an approximation for the bit error probability P_b.

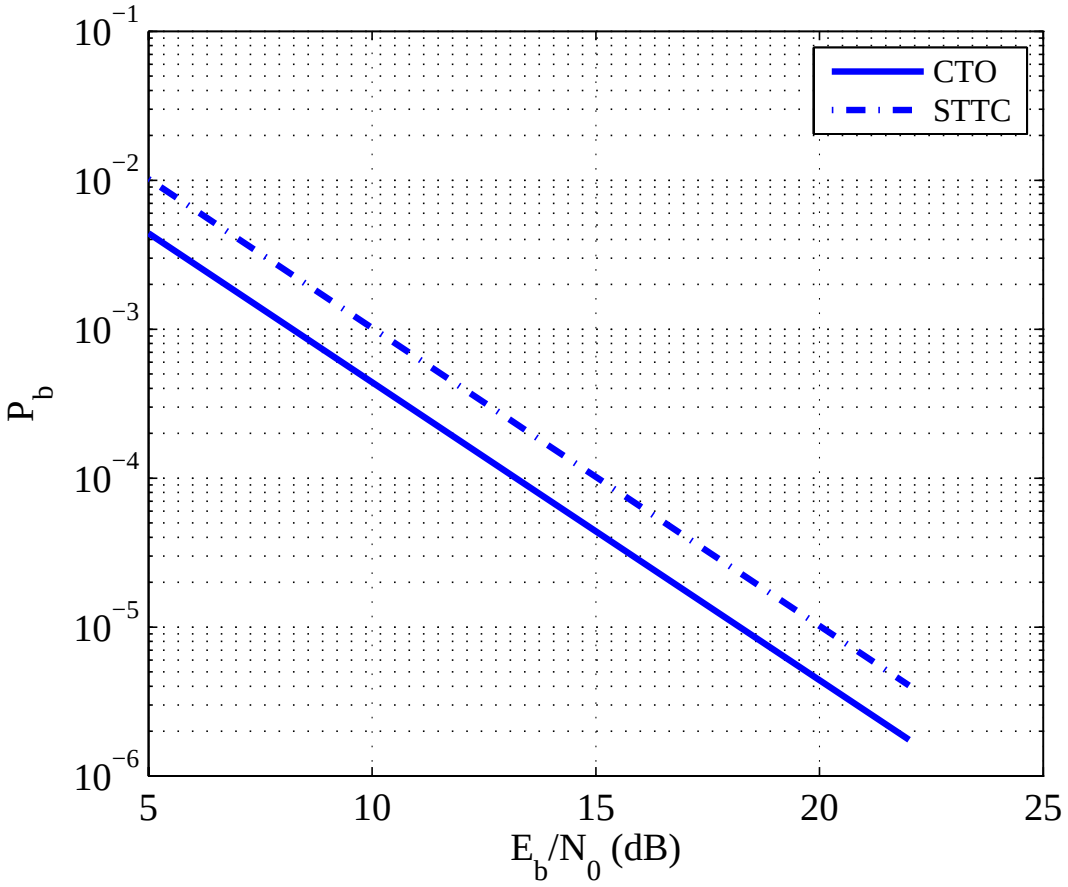

Figure 5.6: The error performance bound comparison between a QPSK CTO system and a QPSK-based smart-greedy STTC system, both of which achieve a rate of 1 bit/ channel use.

To achieve a rate of 2 bits/channel use, a CTO system based on a rate-1/2 trellis code requires

$$2 = \frac{\log_2(M)}{2} \tag{5.16}$$

which requires $M = 16$. For this case, we use the Ungerboeck partitioning of 16-QAM [53]. The third partition produces 8 subsets consisting of 2 constellation points each. (The third partition consists of the "D" subsets shown in Figure 5 of [53].) Each input selects one of the 8 subsets. The two constellation points associated with the selected subset form the two inputs to the Alamouti space-time block code in Figure 5.4 (a).

The probability of error for this system is derived using the equivalent channel suggested by Figure 5.4 (b) and the corresponding 8-state trellis (see Figure 8 of [53]).

The minimum distance error event is associated with $d^2(\mathbf{c}, \mathbf{e}) = 4\sqrt{2}$ and produces 1 bit error.

The average bit error probability for the CTO and STTC systems is illustrated in Figure 5.8. This plot shows that the bit error rate for the CTO system is slightly better than that of the smart-greedy STTC. But, given the approximations used, the most that can be concluded is that the bit error rate performance of the two is comparable.

Again, the number of real-valued multiplications is used to compare the complexity of the two schemes. For an n_s-state trellis code, the decoder requires an n_s-state trellis with $2n_s$ branches at each stage. Each branch metric requires 2 complex-valued multiplications (or 8 real-valued multiplications). The computational load required to produce partial path metrics (including the Alamouti "decoding" computations) is

$$M_{\mathrm{CTO}} = 16n_s + 8 = 136 \tag{5.17}$$

real-valued multiplications for each block of 2 output bits. In comparison, STTC requires a decoder with an n_s-state trellis with $4n_s$ branches. Each branch metric requires 2 complex-valued multiplications (or 8 real-valued multiplications). The computational load required to produce partial path metrics is

$$M_{\mathrm{STTC}} = 32n_s = 256 \tag{5.18}$$

real-valued multiplications for each block of 2 output bits. The ratio $M_{\mathrm{STTC}}/M_{\mathrm{CTO}} \approx 2$ shows that the CTO system is less complex. The complexity comparison are shown in Figure 5.7

Again, the complexity savings is a result of the orthogonalization produced by the Alamouti space-time block code.

5.3 Conclusions

We have demonstrated that a concatenated system based on an orthogonal space-time block code as an outer code and a trellis code as an inner code, optimized

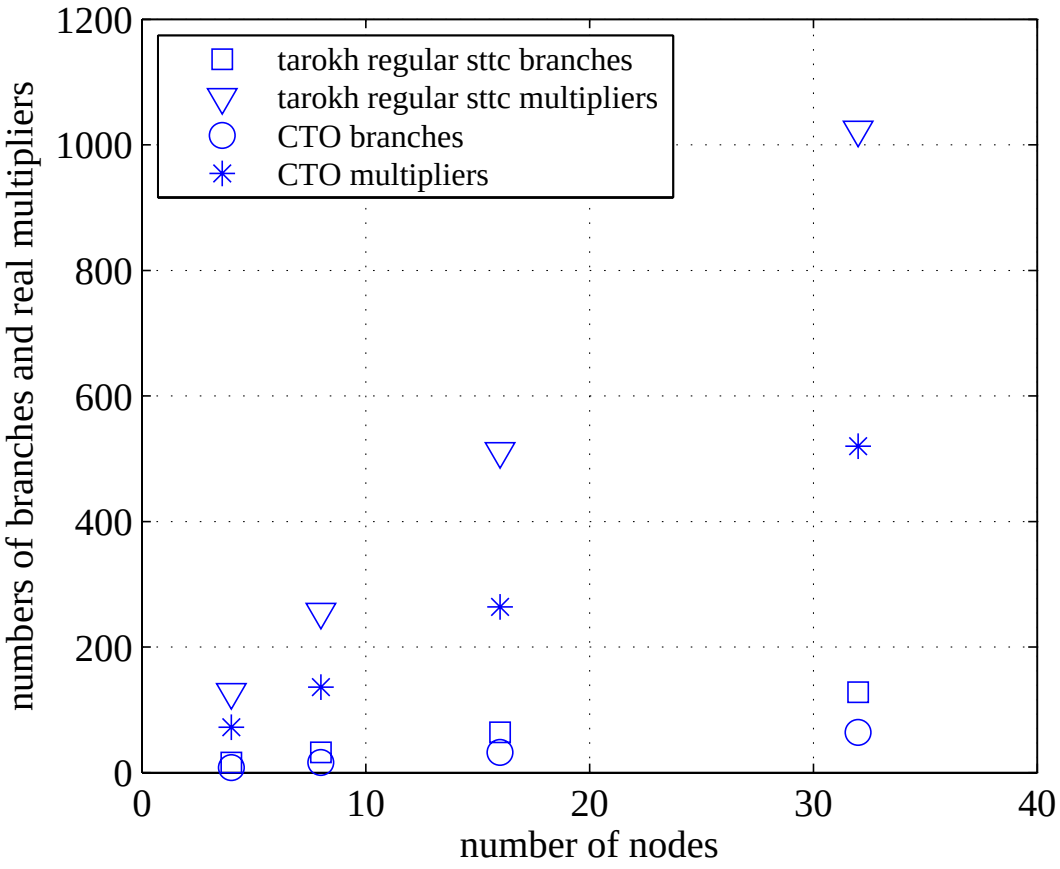

Figure 5.7: The calculation complexity comparison between a QPSK CTO system and a QPSK-based smart-greedy STTC system, both of which achieve a rate of 2 bit/ channel use.

for single-input, single-output fading channel, has a lower BER bound than the space-time trellis code for a 2 by 1 system. It can be also shown from our examples that a concatenated system can save around 4/5 multiplications for the 1 bit per channel use case and around 1/2 multiplications for the 2 bit per channel use case.

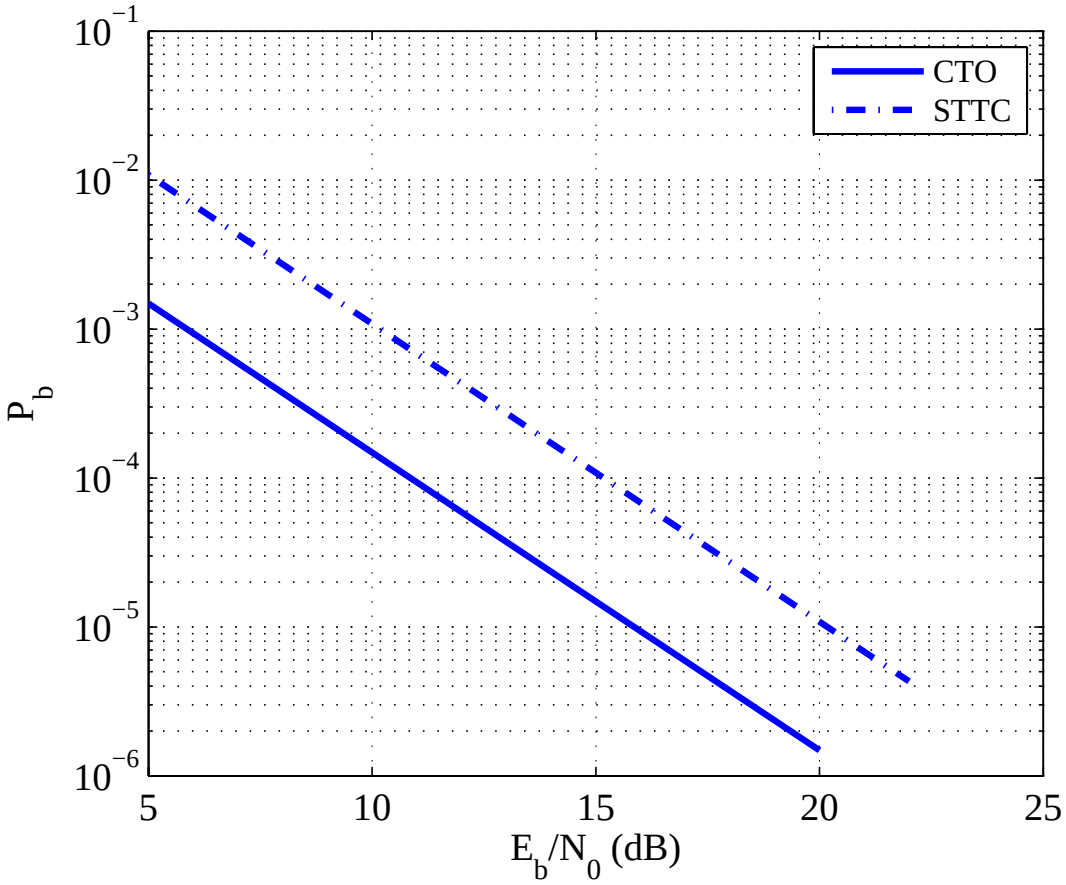

Figure 5.8: The error performance bound comparison between a trellis-coded 16-QAM CTO system and a QPSK-based STTC system, both of which achieve a rate of 2 bit/ channel use.

Chapter 6

Conclusions

In this dissertation, we show how the performance of offset QPSK and ATRM Tier-1 waveforms in SISO could vary with the channel fading parameters. In MIMO environment, in order to expand the symbol-based Alamouti's STBC to the level of packet or waveform, orthogonalization schemes for offset QPSK for MIMO were described and a couple of space-time techniques were compared. The major contributions reported in this dissertation have four parts described in the next section.

6.1 Contributions

In Chapter 2, The bit error rate analysis of offset QSPK over the aeronautical telemetry multipath channel was derived. Simulations show that for the case of a single multipath ray, the BER gets worse with increasing Γ for a fixed delay, and that the BER has a quasi-periodic property for fixed Γ and increasing τ. For the case of two multipath rays, the multipath component characterized by large amplitude and small delay is the main factor of the BER degradation, while the BER is not very sensitive to the change of multipath delay.

In Chapter 3, the bit error rate performance of FQPSK and SOQPSK was derived in the frequency selective multipath fading environment modeled by the aeronautical telemetry channel. A new trellis relationship which decribed the transitions of FQPSK inphase and quadrature waveform pairs were established. Through simulation, we show that in the presence of a strong specular multipath reflection, the ARTM Tier-1 waveforms experience a loss in performance well approximated by (3.27). Simulations of the average bit error probability show that a relatively high error floor at approximately 10^{-2} occurs for $|\Gamma_1| \geq 0.5$.

In Chapter 4, it was shown how orthogonal space-time block codes can be applied *to waveforms* to orthogonalize a space-time coded multiple-input, multiple-output link. For offset QPSK, this technique has the advantage of eliminating the I/Q interference associated with simultaneous transmission of offset QPSK waveforms. As a consequence, a less complex space-time decoder (relative to what would be required without orthogonalization) can be used.

In Chapter 5, it was demonstrated that a concatenated system based on an orthogonal space-time block code as an outer code and a trellis code as an inner code, optimized for single-input, single-output fading channel, has a lower BER bound compared than the space-time trellis code for a 2 by 1 system. It can be also shown from our examples that a concatenated system can save around 4/5 multiplications for the 1 bit per channel use case and around 1/2 multiplications for the 2 bits per channel use case.

6.2 Areas of Future Work

In Chapter 4, we mentioned Cavers' work [1] on space-time trellis coded MSK, where delay diversity is used for the space-time trellis code. One might want to know how MSK would perform with the super-orthogonal space-time trellis code described in [21] where the space-time trellis outer code has an inner space-time orthogonal code, and what performance difference would occur with the concatenated system.

In Chapter 5, We compared a concatenated system based on an orthogonal space-time block code as an outer code and a trellis code as an inner code with an STTC system. It would be interesting to compare between a concatenated system consisting of an orthogonal space-time block code and a trellis code modulation [53] of other signal like 8-PSK constellations with an STTC system, also to compare the concatenated system consisting of an orthogonal space-time block code and bit interleaved coded modulation (BICM) [54] [55] with an STTC system.

Slow fading channel is assumed in both Chapter 4 and Chapter 5. The analysis and performance of the described scheme in fast fading channels can be further studied.

Bibliography

[1] J. K. Cavers, "Space-time coding using MSK," *IEEE Transactions on Wireless Communications*, vol. 4, no. 1, pp. 185–191, Jan 2005. xx, 2, 4, 6, 9, 45, 46, 55, 59, 80

[2] V. Tarokh, N. Seshadri, and A. Calderbank, "Space-time codes for high data rate wireless communication: Performance criterion and code construction," *IEEE Transactons on Information Theory*, vol. 44, no. 2, pp. 744–765, Mar 1998. xx, 2, 4, 7, 45, 63, 65, 67, 70, 72

[3] A. Silvester, R. Schober, and L. Lampe, "Burst-based orthogonal ST block coding for CPM," *IEEE Transactions on Wireless Communications*, vol. 6, no. 4, pp. 1208 – 1212, April 2007. xx, 4, 45, 46, 63, 65, 68

[4] M. Simon, *Bandwidth-efficient digital modulation with application to deep-space communications*. Hoboken, NJ: John Wiley & Sons, 2003. 1, 3

[5] *IRIG Standard 106-00: Telemetry Standards*, Range Commanders Council Telemetry Group, Range Commanders Council, White Sands Missile Range, New Mexico, 2000, (Available on-line at http://jcs.mil/RCC/manuals/106-00). 1, 25

[6] W. Gao and K. Feher, "FQPSK: A bandwidth and RF power efficient technology for telemetry applications," in *Proceedings of the International Telemetering Conference*, Las Vegas, NV, October 1997, pp. 480–488. 1, 23

[7] T. Hill, "An enhanced, constant envelope, interoperable shaped offset QPSK (SOQPSK) waveform for improved spectral efficiency," in *Proceedings of the International Telemetering Conference*, San Diego, CA, October 2000, pp. 127–136. 1, 3, 23, 41

[8] E. Law and K. Feher, "FQPSK versus PCM/FM for aeronautical telemetry applications; spectral occupancy and bit error probability comparisons," in *Proceedings of the International Telemetering Conference*, Las Vegas, NV, October 1997, pp. 489–496. 1, 23

[9] M. Rice, A. Davis, and C. Bettwieser, "A wideband channel model for aeronautical telemetry," *IEEE Transactions on Aerospace and Electronic Systems*, vol. 37, no. 1, January 2004. 2, 3, 12, 23, 25, 31, 38

[10] S. Alamouti, "A simple transmit diversity techniques for wireless communications," *IEEE Journal on Selected Areas in Communications*, vol. 16, no. 8, pp. 1451–1458, Oct 1998. 2, 3, 5, 45, 68

[11] V. Tarokh, H. Jafarkhani, and A. Calderbank, "Space-time block codes from orthogonal designs," *IEEE Transactions on Information Theory*, vol. 45, pp. 1456–1467, July 1999. 2, 45, 53, 63

[12] T. Nelson and M. Rice, "Detection of offset QPSK with unitary space-time block codes," to appear in *IEEE Transactions on Communications*. 2, 4

[13] M. Rice, "PCM/FM aeronautical telemetry in frequency selective multipath interference," *IEEE Transactions on Aerospace and Electronic Systems*, vol. 36, no. 4, pp. 1090–1098, October 2000. 2, 24, 38

[14] K. Feher and S. Kato, U. S. Patent 4,567.602; K. Feher, U. S. Patent 5,491,457; K. Feher, U.S. Patent 5,784,402. 3, 24

[15] T. Hill, "Performance of SOQPSK and multi-h CPM in the presence of adjacent channel interference," in *Proceedings of the International Telemetering Conference*, Las Vegas, NV, October 2001, pp. 255–263. 3

[16] M. Geoghegan, "Optimal linear detection of SOQPSK," in *Proceedings of the International Telemetering Conference*, San Diego, CA, October 2002. 3, 42

[17] T. Nelson, E. Perrins, and M. Rice, "Near optimal common detection techniques for shaped offset QPSK and Feher's QPSK," *IEEE Transactions on Communications*, vol. 56, 2008. 3

[18] X. Zhang and M. Fitz, "Space-time code design with continuous phase modulation," *IEEE Journal on Selected Areas in Communications*, vol. 21, no. 5, pp. 783–792, Jun 2003. 4, 45

[19] G. Wang and X. Xia, "An orthogonal space-time coded CPM system with fast decoding for two transmit antennas," *IEEE Transactions on Information Theory*, vol. 50, pp. 486–493, March 2004. 4, 45

[20] U. aygolu and M. Celebi, "Space-time MSK codes for quasi-static fading channel," *Int. J. Eletron. Comm.*, vol. 58, no. 4, pp. 268–273, 2004. 4, 45

[21] H. Jafarkhani and N. Seshadri, "Super-orthogonal space-time trellis codes," *IEEE Transactions on Information Theory*, vol. 49, no. 4, pp. 937 – 950, Apr 2003. 5, 80

[22] S. Siwamogsatham and M. P. Fitz, "High-rate concatenated space-time block code m-tcm designs," *IEEE Transactions on Information Theory*, vol. 51, no. 12, pp. 4173–4183, 2005. 5

[23] Y. Li, P. Fung, Y. Wu, and S. Sun, "Performance analysis of mimo system with serial concatenated bit-interleaved coded modulation and linear dispersion code," in *Communications, 2004 IEEE International Conference on*, 2004, pp. 692–696. 5

[24] E. C. Page, "Binary decoding of concatenated turbo codes and space-time block codes for quaternary modulations," in *Electrotechnical Conference, 2004. MELECON 2004. Proceedings of the 12th IEEE Mediterranean*, May 2004, pp. 1159 – 1164. 5

[25] Y. Gong and K. B. Letaief, "Concatenated spacectime block coding with trellis coded modulation in fading channels," *IEEE TRANSACTIONS ON WIRELESS COMMUNICATIONS*, vol. 1, no. 4, pp. 580–590, Oct 2002. 5, 6, 7

[26] T. Yong, W. Junli, L. Tao, and Y. Guangxin, "Concatenated space-time block code with trellis coded modulation in ofdm system," in *Communication Technology Proceedings, 2003. ICCT 2003. International Conference on*, Apr 2003, pp. 1194 – 1197. 6, 7

[27] K. aksoy and U. Aygolu, "An efficient concatenated trellis code and coordinate interleaved orthogonal design for mimo ofdm," *International Journal of Electronics and Communications*, 2009. 6

[28] S. Sandhu, R. Heath, and A. Paulraj, "Space-time block codes versus space-time trellis codes," in *Proceedings of the IEEE International Communications Conference*, Helsinki, Finland, 11–14 June 2001, pp. 1132–1136.

[29] M. Rice and X. Dang, "An analysis of FQPSK and SOQPSK in frequency selective multipath," in *Proceedings of the Military Communications Conference*, October 2004, pp. 78 – 84. 8

[30] ——, "Aeronautical telemetry using offset qpsk in frequency selective multipath," *IEEE Transactions on Aerospace and Electronic Systems*, vol. 41, no. 2, pp. 758 – 767, Apr 2005. 8

[31] X. Dang and M. Rice, "On space-time trellis-coded offset QPSK," in *Proceedings of the IEEE International Conference on Communications*, Beijing, China, May 2008. 8, 70, 72

[32] ——, "Space-time trellis codes and concatenated trellis-coded orthogonal space-time block codes: A performance and complexity comparison," submitted to IEEE Globecomm, 2009. 8

[33] C. Irving, "Range telemetry improvement and modernization," in *Proceedings of the International Telemetering Conference*, Las Vegas, NV, October 1997, pp. 294 – 303. 23

[34] S. Kato and K. Feher, "XPSK: A new cross-correlated phase-shift-keying modulation technique," *IEEE Transactions on Communications*, vol. 31, no. 5, pp. 701 –707, May 1983. 24

[35] M. Simon, *Bandwidth-Efficient Digital Modulation with Application to Deep Space Communications*. Wiley-Interscience, 2003. 24, 25, 26

[36] J. Proakis, *Digital Communications*. McGraw-Hill, 2001. 30, 31, 56, 57

[37] J. Anderson, T. Aulin, and C.-E. Sundberg, *Digital Phase Modulation*. New York: Plenum Press, 1986. 41

[38] A. Svensson and C.-E. Sundberg, "Optimum MSK-type receivers for CPM on Gaussian and Rayleigh fading channels," *IEE Proceedings*, pp. 480–490, August 1984. 42

[39] ——, "Serial MSK-type detection of partial response continuous phase modulation," *IEEE Transactions on Communications*, vol. 33, no. 1, pp. 44–52, January 1985. 42

[40] P. Galko and S. Pasupathy, "Optimization of linear receivers for data communication signals," *IEEE Transactions on Information Theory*, vol. 34, no. 1, pp. 79–92, January 1988. 42

[41] ——, "Linear receivers for correlatively coded MSK," *IEEE Transactions on Communications*, vol. 33, no. 4, pp. 338–347, April 1985. 42

[42] R. Rhodes, S. Wilson, and A. Svensson, "MSK-type reception of continuous phase modulation: Cochannel and adjacent channel interference," *IEEE Transactions on Communications*, vol. 35, no. 2, pp. 185–193, February 1987. 42

[43] C. Cheng and C. Lu, "Space-time code design for CPFSK modulation over frequency-nonselective fading channel," *IEEE Transactions on Communications*, vol. 53, no. 12, pp. 413–416, Dec 2005. 45

[44] R. H.-H. Yang *et al.*, "Space-time coded GMSK for wireless communication," in *Proceedings of the IEEE International Symposium on Intelligent Signal Processing and Communication Systems*, December 2005, pp. 413–416. 45

[45] I. Altunbas, "Space-time trellis codes for MSK," *Computers and Elctrical Engineering*, vol. 31, no. 4, pp. 263–271, 2005. 45

[46] P. Laurent, "Exact and approximate construction of digital phase modulations by superposition of amplitude modulated pulses (AMP)," *IEEE Transactions on Communications*, vol. 34, pp. 150–160, Feb 1986. 45

[47] Y. Yao and M. Howlader, "Serial concatenated MSK modulated space-time block coding," in *Proceedings of the IEEE International Communications Conference*, Paris, France, June 2004, pp. 3015–3019. 45

[48] T. Nelson and M. Rice, "Detection of SOQPSK in a space-time coded system with arrival time differences," in *Proceedings of IEEE Military Communications Conference*, Monterey, CA, November 2004. 46

[49] M. Jensen, M. Rice, T. Nelson, and A. Anderson, "Orthogonal dual-antenna transmit diversity for SOQPSK in aeronautical telemetry channels," in *Proceedings of the International Telemetering Conference*, San Diego, CA, October 2004, pp. 337–344. 46

[50] T. Nelson and M. Rice, "MIMO communications using offset modulations," in *Proceedings of the IEEE International Waveform Diversity and Design Conference*, Lihue, HI, 23 - 27 January 2006. 46

[51] ——, "Detection of offset QPSK with unitary space-time block codes," in *Proceedings of the IEEE Global Communications Conference*, Washington, DC, November 2007. 46

[52] P. Frenger, P. Orten, and T. Ottosson, "Convolutional codes with optimum distance spectrum," *IEEE Communications Letters*, vol. 3, no. 11, pp. 317–319, 1999. 58

[53] G. Ungerboeck, "Channel coding with multilevel/phase signals," *IEEE Transactions on Information Theory*, vol. 28, no. 1, pp. 701 –707, January 1982. 74, 80

[54] E. Zehavi, "8-PSK trellis codes for a Rayleigh channel," *IEEE Transactions on Communications*, vol. 40, no. 5, pp. 873 – 884, May 1992. 80

[55] G. Caire, G. Taricco, and E. Biglieri, "Bit-interleaved coded modulation," *IEEE Transactions on Information Theory*, vol. 44, no. 3, pp. 927 – 949, May 1998. 80